An analytic formula for entraining CAPE in mid-latitude storm environments

John M. Peters[a] , Daniel R. Chavas[b] , Chun-Yian Su[a] , Hugh Morrison[c] , and Brice E. Coffer[d]

[a] *Department of Meteorology and Atmospheric Science, The Pennsylvania State University, University Park, PA*

[b] *Department of Earth, Atmospheric, and Planetary Sciences, Purdue University, West Lafayette, IN*

[c] *National Center for Atmospheric Research, Boulder, CO*

[d] *Department of Marine, Earth and Atmospheric Sciences, North Carolina State University, Raleigh, NC*

Corresponding author: John M. Peters, John.M.Peters@psu.edu

Early Online Release: This preliminary version has been accepted for publication in *Journal of the Atmospheric Sciences*, may be fully cited, and has been assigned DOI 10.1175/JAS-D-23-0003.1. The final typeset copyedited article will replace the EOR at the above DOI when it is published.

ABSTRACT: This article introduces an analytic formula for entraining convective available potential energy (ECAPE) with an entrainment rate that is determined directly from an environmental sounding, rather than prescribed by the formula user. Entrainment is connected to the background environment using an eddy diffusivity approximation for lateral mixing, updraft geometry assumptions, and mass continuity. These approximations result in a direct correspondence between the storm relative flow and the updraft radius and an inverse scaling between the updraft radius squared and entrainment rate. The aforementioned concepts, combined with the assumption of adiabatic conservation of moist static energy, yield an explicit analytic equation for ECAPE that depends entirely on state variables in an atmospheric profile and a few constant parameters with values that are established in past literature. Using a simplified Bernoulli-like equation, the ECAPE formula is modified to account for updraft enhancement via kinetic energy extracted from the cloud's background environment. CAPE and ECAPE can be viewed as predictors of the maximum vertical velocity w_{max} in an updraft. Hence, these formulas are evaluated using w_{max} from past numerical modeling studies. Both of the new formulas improve predictions of w_{max} substantially over commonly used diagnostic parameters, including undiluted CAPE and ECAPE with a constant prescribed entrainment rate. The formula that incorporates environmental kinetic energy contribution to the updraft correctly predicts instances of exceedance of $\sqrt{2\text{CAPE}}$ by w_{max}, and provides a conceptual explanation for why such exceedance is rare among past simulations. These formulas are potentially useful in nowcasting and forecasting thunderstorms and as thunderstorm proxies in climate change studies.

Accepted for publication in *Journal of the Atmospheric Sciences*. DOI 10.1175/JAS-D-23-0003.1.

SIGNIFICANCE STATEMENT: Substantial mixing occurs between the upward moving air currents in thunderstorms (updrafts) and the surrounding comparatively dry environmental air, through a process called entrainment. Entrainment controls thunderstorm intensity via its diluting effect on the buoyancy of air within updrafts. A challenge to representing entrainment in forecasting and predictions of the intensity of updrafts in future climates is to determine how much entrainment will occur in a given thunderstorm environment without a computationally expensive high resolution simulation. To address this gap, this article derives a new formula that computes entrainment from the properties of a single environmental profile. This formula is shown to predict updraft vertical velocity more accurately than past diagnostics, and can be used in forecasting and climate prediction to improve predictions of thunderstorm behavior and impacts.

1. Introduction

Middle-to-upper tropospheric vertical velocities[1] in deep convective updrafts influence a variety of storm-related societal impacts, including precipitation (e.g., Jo and Lasher-Trapp 2022), hail (e.g., Danielsen et al. 1972; Lin and Kumjian 2022), electrification (e.g., Romps et al. 2014; Stolz et al. 2015), downdraft and cold pool intensity (e.g., Marion and Trapp 2019), tropospheric convective mass flux (e.g., Peters et al. 2021), and the flux of mass, aerosols, and water vapor across the tropopause (e.g., Mullendore et al. 2013). The magnitude of vertical velocities in the upper reaches of deep convective updrafts are strongly influenced by updraft buoyancy (e.g., Morrison and Peters 2018; Peters et al. 2019; Jeevanjee 2017). It is well known that entrainment-driven dilution of deep convective updrafts substantially influences updraft buoyancy and vertical velocity (e.g., Zipser 2003; Romps and Kuang 2010a,b). For instance, weakly sheared deep convective updrafts with large fractional entrainment rates are substantially diluted and often only realize a small fraction (e.g., 20-30 %) of their convective available potential energy (CAPE) as updraft kinetic energy (Romps and Kuang 2010a). In contrast, more organized modes of deep convection such as squall lines and supercells with smaller fractional entrainment rates and less dilution can realize much larger fractions of their CAPE as KE (i.e., 80-100 %; Lebo and Morrison 2015; Peters et al. 2019; Mulholland et al. 2021b). Hence, storm-to-storm variations in entrainment substantially alter how much CAPE a storm is able to process, and consequently its updraft kinetic energy and vertical

[1]We contrast middle-to-upper tropospheric vertical velocities, which are primarily buoyantly driven, with lower tropospheric vertical velocities which are often dynamically driven in squall lines (e.g., Bryan and Rotunno 2014; Jeevanjee and Romps 2015) and supercells (e.g., Weisman and Rotunno 2000; Peters et al. 2019).

Accepted for publication in *Journal of the Atmospheric Sciences*. DOI 10.1175/JAS-D-23-0003.1.

velocity. These storm-to-storm variations in entrainment also generally supersede the influences of variations in other updraft processes and environment factors on vertical velocity that have received substantial attention in the literature (e.g., Lebo 2018; Grabowski and Morrison 2021), such as aerosol effects, pressure perturbations, and precipitation behavior. Hence, the atmospheric science community would benefit from an accurate representation of entrainment in diagnostic parameters such as CAPE to improve our ability to characterize the intensity of convective updrafts that might form in a given environment.

CAPE calculations that include entrainment effects are referred to as entraining CAPE, or ECAPE. Whereas CAPE is often viewed as the theoretical maximum kinetic energy that can be extracted by an isolated parcel from its environment via buoyant acceleration, ECAPE makes additional assumptions about updraft steadiness and mixing to estimate how the efficiency of this kinetic energy extraction is affected by entrainment. Various ECAPE-like calculations have been used for the better part of the last century, primarily in the climate, tropical meteorology, and cumulus parameterization communities. For instance, simple plume models (e.g., Squires and Turner 1962) for moist convective updrafts predict profiles of buoyancy that include entrainment effects, which can be vertically integrated to obtain ECAPE. The "cloud work function", which is an essential element of many cumulus parameterizations (Arakawa and Schubert 1974), uses the buoyancy of a diluted parcel within its calculation, and yields a quantity that is analogous to ECAPE. ECAPE is used as diagnostic tool in the research of tropical environments to explain the sensitivity of deep convection initiation to free tropospheric moisture (Brown and Zhang 1997), and in the closure formulation of cumulus parameterizations (Zhang 2009). The zero-buoyancy plume model, in which buoyancy is assumed to be exactly extinguished by entrainment, yields analytic solutions for the mean state thermal structure of the tropical atmosphere (Singh and O'Gorman 2013). The range of fractional entrainment rates in the tropics is typically smaller than that of the mid latitudes (e.g., Takahashi et al. 2021). Hence, using an ECAPE calculated with an empirically obtained constant fractional entrainment rate provides reasonably accurate predictions of deep convective updraft characteristics in the tropics (e.g., Gregory 2001)

There are also a few scattered applications of ECAPE in the weather forecasting community. For instance, the spatial distribution of ECAPE has been shown to better identify the tornadic regions of tropical (Sueki and Niino 2016) and extratropical cyclones (Tochimoto et al. 2019) than undiluted

Accepted for publication in *Journal of the Atmospheric Sciences*. DOI 10.1175/JAS-D-23-0003.1.

CAPE. ECAPE has also been used to predict vertical velocities in supercells more accurately than standard CAPE calculations (Peters et al. 2020a). There is substantially larger variability in fractional entrainment in the continental mid-latitudes (e.g., Peters et al. 2020b; Takahashi et al. 2021; Lasher-Trapp et al. 2021) than in the tropics, meaning that ECAPE computed with a single fractional entrainment rate cannot accurately describe all midliatude convective environments (e.g., Peters et al. 2020b). This makes using ECAPE in midlatudes more difficult than in the tropics, because it is not always clear what entrainment rate should be used in the calculation.

To address the issue of what choice of fractional entrainment rate to use in the midlatitudes, Peters et al. (2020a) (hereafter P20) developed an analytic formula for maximum updraft vertical velocity (which is equal to $\sqrt{2ECAPE}$) that calculated entrainment from attributes of a storm's background environment, rather than requiring that the user specify an entrainment rate. The connection between entrainment and the background environment in this formula was based on a conceptual model developed in Peters et al. (2019). In this conceptual model, a mature updraft's radius, and consequently its fractional entrainment rate, are determined by its low-level environmentally-driven inflow via mass continuity. Low-level inflow strongly corresponds with low-level storm-relative flow (e.g., Peters et al. 2019, 2020b, 2022b) — the latter of which is predictable from an environmental wind profile (Bunkers et al. 2000) and correlates with the magnitude of vertical wind shear (Peters et al. 2020b). P20 leveraged these connections to use the environmental wind profile to predict the updraft radius and fractional entrainment rate. This formula more accurately predicted maximum updraft vertical velocities than standard ECAPE computed with a constant pre-specified fractional entrainment rate.

There are several shortcomings of the P20 study that warrant a revisit of the concepts contained therein. First, the expression derived in the paper uses a hodgepodge of formulas from previous studies, such as Morrison (2017) and Peters et al. (2019) as a starting point[2]. The assumptions underlying these formulas from previous studies are not explicitly discussed in P20, nor are they even thoroughly scrutinized in their source articles. Because of this rooting in past studies, a few of the terms that end up in the P20 equation are complicated and lack obvious physical underpinning, which is challenging for end users of this formula.

[2]Note a litany of constants are carried over into P20 from these past formulas, and some of the symbols used (such as H_v for the latent heat of vaporization) are inconsistent with the symbols used in some of our more recent articles (e.g., L_v for the latent heat of vaporization; Peters and Chavas 2021; Peters et al. 2022c,a).

Accepted for publication in *Journal of the Atmospheric Sciences*. DOI 10.1175/JAS-D-23-0003.1.

Second, the end formula for maximum updraft vertical velocity is a third-order polynomial equation that must either be solved explicitly with the complicated quartic equation, or with a numerical root finding procedure. End users of the formula found this quartic solution difficult to efficiently incorporate into software routines. This 3rd order polynomial equation results from the assumption that fractional entrainment ε scales with the inverse of updraft radius R^{-1}. However, there is now evidence that $\varepsilon \sim R^{-2}$ is a more realistic scaling (Peters et al. 2019; Morrison et al. 2022; Mulholland et al. 2021b). Re-formulating the P20 equation with $\varepsilon \sim R^{-2}$ yields a 2nd-order polynomial equation that is much easier to solve, as will be shown in the present study.

While not a science consideration, the title of that paper, which is "A formula for the maximum vertical velocity in supercell updrafts", obscures the take-home message of that article. The title does not contain the terms entrainment or CAPE, so it is not obvious that the parameter derived in the paper essentially modifies CAPE to account for the effects of entrainment (which is by definition ECAPE). The concepts contained within the paper apply to any isolated deep convective updraft existing within moderate to strong vertical wind shear – they are not limited to supercells. There is no assumption about updraft rotation within the mathematical framework. Hence, the inclusion of the term supercell in the title made the application of the formula sound unnecessarily restrictive, and an ancillary objective of the present article is to better convey the general applicability of the formula (i.e., beyond supercells) within research and forecast activities that presently rely upon undiluted CAPE for analysis and forecasting.

Our goal in this article is to revisit the concepts of P20 to derive an ECAPE formula (Sections 2-3) that improves upon the concepts in the P20 study in the following ways:

1. The buoyancy formula in the present study is derived directly from the assumed conservation of moist static energy, which differs from the P20 formula which used the supersaturation tendency equation from Politovich and Cooper (1988) as a starting point. This methodological alteration requires less severe assumptions and results in formulas with greater accuracy in the present study.

2. The new formula uses the $\varepsilon \sim R^{-2}$ scaling, with further improves accuracy over the P20 formula.

Accepted for publication in *Journal of the Atmospheric Sciences*. DOI 10.1175/JAS-D-23-0003.1.

3. We also account for additional processes that were not considered by P20, such as the contribution to updraft kinetic energy from the kinetic energy an updraft extracts from its inflow via pressure gradient accelerations.

The new ECAPE formula is evaluated with output from four past numerical modeling studies that included 141 simulations (Section 4). The formulas and their constituent terms, along with recommended parameter values, are summarized in the discussion and conclusions (Section 5).

2. Derivation of analytic ECAPE formula

a. Overview of deviation, in words

This section contains a detailed derivation of the ECAPE formula from first principles. Readers who are uninterested in these technical details may consider simply reading this subsection and then skipping to section 3, which provides the computation steps required to compute ECAPE (section 3a) and evaluates the formula against past simulations (section 3b), and explores the behavior of ECAPE in past soundings from severe weather events (section 3c).

The derivation relies on four underlying concepts:

1. An eddy diffusivity approximation for the lateral mixing between an updraft and the environment (section 2c), which yields an inverse squared scaling between entrainment and updraft radius.

2. The assumption that moist static energy (a close cousin to equivalent potential temperature) is diluted in a manner akin to that of a passive tracer as a parcel rises through an updraft and mixes with the surrounding environment (section 2d). This yields an analytic relationship between ECAPE and entrainment.

3. The assumption that an updraft's inflow is determined by the low-level environmental storm-relative wind speed, which yields analytic relationship between updraft radius and state variables within an atmospheric sounding (sections 2e-f).

4. The assumption that kinetic energy is conserved along inflow that enters the low-level updraft and is deflected upward (section 2g).

Accepted for publication in *Journal of the Atmospheric Sciences*. DOI 10.1175/JAS-D-23-0003.1.

Combining these components allows us to eliminate entrainment and updraft radius from the system of equations to express ECAPE as a function of the state variables within a sounding.

b. Methods for evaluating our derived formulas

We will need to make several approximations through the course of the derivation. To evaluate the accuracy of these approximations, we will first establish a *benchmark calculation* of both buoyancy and ECAPE computed with *as few approximations as possible*. For instance, the benchmark calculation includes the temperature dependency of latent heat, the hydrometeor dependency of the moist heat capacity, and virtual temperature and condensate loading effects in buoyancy calculations. Profiles of benchmark buoyancy are calculated by numerically integrating the adiabatic unsaturated and saturated lapse rate equations derived in Peters et al. (2022c), eqs. 19 and 24 from that article respectively, with a mixed-phase layer in the parcel temperature range of 273.5 K to 233.15 K (see that study for details on the mixed-phase calculation), and allows the user to specify a constant-with-height fractional entrainment rate that controls the rate at which the parcel mixes with the horizontally invariant background environment (see eq. 36-38 in that study).

The formulas are evaluated using the severe weather proximity sounding dataset of Thompson et al. (2003). This dataset includes 1028 atmospheric profiles taken near severe weather events that ranged from disorganized deep convection to tornadic supercells. In each profile, the parcel with the largest undiluted CAPE in the lowest 5 km of the atmosphere is lifted to calculate buoyancy, CAPE, and ECAPE.

c. Connecting fractional entrainment to updraft radius

Our first derivation step is to establish a relationship between updraft radius and the fractional entrainment rate ε. The derivation closely follows that of Morrison (2017) (hereafter M17), section 2a therein. We first consider a passive tracer C, whose mixing ratio (in kg kg^{-1}) is 1 in a cloud's effective inflow layer (i.e., the layer of nonzero CAPE; Thompson et al. 2007; Nowotarski et al. 2020), and 0 above this layer. Conceptually, the passive tracer value represents the amount of dilution a parcel has experienced, with $C \approx 1$ indicating undiluted air, and $0 \leq C << 1$ indicating highly diluted air.

Accepted for publication in *Journal of the Atmospheric Sciences*. DOI 10.1175/JAS-D-23-0003.1.

The anelastic Lagrangian tendency equation for C may be written in cylindrical coordinates as:

$$\frac{dC}{dt} = \frac{\partial C}{\partial t} + \frac{1}{r}\frac{\partial ruC}{\partial r} + \frac{1}{r}\frac{\partial vC}{\partial \phi} + \frac{1}{\rho_0}\frac{\partial \rho_0 wC}{\partial z} = 0, \tag{1}$$

where r, ϕ, and z are the radial, azimuthal, and vertical coordinates ($r = 0$ is the updraft core), u, v, and w are the corresponding radial, azimuthal, and vertical velocities, and $\rho_0(z)$ is a reference density profile. Azimuthally averaging this equation, and then Reynolds averaging, yields:

$$\frac{\bar{d}\bar{C}}{dt} = -\frac{1}{r}\frac{\partial r\overline{u'C'}}{\partial r} - \frac{1}{\rho_0}\frac{\partial \overline{\rho_0 w'C'}}{\partial z} \tag{2}$$

where overbars denote smoothed four-dimensional fields with a spatial filter scale similar to that of a typical deep convective updraft width (i.e., 1-2 km), primes denote deviations smaller than the filter scale, and $\frac{\bar{d}\bar{C}}{dt} \equiv \frac{\partial \overline{C}}{\partial t} + \frac{1}{r}\frac{\partial r\overline{u}\overline{C}}{\partial r} + \frac{1}{r}\frac{\partial \overline{v}\overline{C}}{\partial \phi} + \frac{\partial \overline{w}\overline{C}}{\partial z}$. Physically, the overbar terms correspond to updraft-scale flow patterns, whereas the $'$ terms correspond to turbulent fluxes. We neglect the vertical turbulent flux term since recent large eddy simulations have supported a dominant role of lateral mixing in entrainment (Böing et al. 2014). All quantities are valid at the updraft horizontal center unless explicitly stated otherwise.

Following M17 and De Rooy and Siebesma (2010), we assume that $\overline{u'C'}$ varies linearly over a turbulent mixing length scale L_{mix} and vanishes at the updraft center, such that $\overline{u'C'}(r) = \overline{u'C'}\Big|_{L_{mix}}\left(\frac{r}{L_{mix}}\right)$, where $\overline{u'C'}\Big|_{L_{mix}}$ denotes the value of $\overline{u'C'}$ at distance L_{mix} from the updraft center. Finally, we use the chain rule to write $\frac{\bar{d}}{dt} = \overline{w}\frac{\bar{d}}{dz}$, where $\frac{\bar{d}}{dz}$ is the rate of change of a quantity as the parcel changes height. Making these approximations allows us to write eq. 2 as:

$$\frac{\overline{dC}}{dz} = -2\frac{\overline{u'C'}\Big|_{L_{mix}}}{\overline{w}L_{mix}}. \tag{3}$$

In the eddy diffusivity approximation (e.g., Kuo 1962), we assume that turbulent fluxes act to diffuse a quantity down-gradient. Using this approach, we may write $\overline{u'C'}\Big|_{L_{mix}} \approx -\frac{k^2 L_{mix}^2}{P_r}\left|\frac{\partial w}{\partial r}\right|\frac{\partial C}{\partial r}$

Accepted for publication in *Journal of the Atmospheric Sciences*. DOI 10.1175/JAS-D-23-0003.1.

(eqs. 5-6 in M17)[3] and eq. 3 as:

$$\overline{\frac{dC}{dz}} = 2\frac{k^2 L_{mix}}{\overline{w} P_r}\left|\frac{\partial w}{\partial r}\right|\frac{\partial C}{\partial r}, \tag{4}$$

where k is the von Karman constant and P_r is the turbulent Prandtl number. Finally, we use linear approximations to the lateral gradients in C and w, such that $\frac{\partial C}{\partial r} = \frac{C_0 - \overline{C}}{R}$ and $\left|\frac{\partial w}{\partial r}\right| = \frac{|w_0 - \overline{w}|}{R}$, where $w_0 = 0$ m s^{-1} and $C_0 = 0$ are vertical velocity and tracer values in the background environment. These approximations give:

$$\overline{\frac{dC}{dz}} = -\varepsilon \overline{C}, \tag{5}$$

where

$$\varepsilon = \frac{2k^2 L_{mix}}{P_r R^2}. \tag{6}$$

Equation 5 takes the form of a classical steady-state plume equation (Squires and Turner 1962; Betts 1975), where ε is the fractional entrainment inverse length scale. This term represents the rate at which C is diluted with height by entrainment. There is some debate in past literature over how L_{mix} should be interpreted. For instance, in Morrison et al. (2020), P20, and Peters et al. (2021), we simply set $L_{mix} \sim R$, which from Equation 6 results in a $\varepsilon \sim R^{-1}$ scaling. However, analysis of large eddy simulations (LES) in our more recent work (e.g., Mulholland et al. 2021b; Morrison et al. 2022) indicates that $\varepsilon \sim R^{-2}$, suggesting from Equation 6 that L_{mix} should be viewed as a constant. Hence, we set L_{mix} to a fixed value that is independent of R, following Morrison et al. (2022).

The eddy diffusivity approximation for lateral mixing implicitly neglects the entrainment of air occurring within organized updraft-scale flow, which is known as dynamic entrainment (e.g., De Rooy et al. 2013). However, our past work has shown that dynamic entrainment primarily affects updraft properties below the height of maximum w where flow is laterally convergent into the updraft (e.g., Morrison 2017; Morrison et al. 2020, 2022). For instance, see the schematics in Figs. 15 and 4 in Morrison (2017) and Morrison et al. (2020) respectively for the conceptual basis of this assumption, which yields accurate predictions of the profiles of atmospheric quantities along trajectories in simulations (see Fig,. 8 in Peters et al. 2022c). Hence, it is reasonable to

[3]Physically, the $|\frac{\partial w}{\partial r}|$ term indicates that horizontal turbulent mixing will be enhanced in the presence of strong horizontal velocity gradients and the associated shear instability (e.g., Kuo 1962) .

Accepted for publication in *Journal of the Atmospheric Sciences*. DOI 10.1175/JAS-D-23-0003.1.

neglect dynamic entrainment in our present objective of deriving an expression for ECAPE, which pertains to the maximum kinetic energy achieved by the updraft that coincides with the position of maximum w.

d. Derivation of analytic expressions for the buoyancy and ECAPE of an entraining parcel

Our next step is to express ECAPE as an analytic function of ε. Later, we will combine this ECAPE expression with eq. 6 to eliminate ε and express ECAPE as a function of R. We begin with the first law of thermodynamics for a rising parcel, which may be written as (e.g., Emanuel 1994; Romps 2015; Peters et al. 2022c):

$$c_{pm}\frac{dT}{dz} - \frac{1}{\rho}\frac{dp}{dz} + L_v\frac{dq_v}{dz} - L_i\frac{dq_i}{dz} = Q \tag{7}$$

where c_{pm} is the moist heat capacity that depends on water vapor and condensates, T is temperature, ρ is density, p is pressure, L_v is the temperature dependent latent heat of vaporization, q_v is the water vapor mass fraction, L_i is the temperature dependent latent heat of freezing, q_i is the ice mass fraction[4], Q represents all diabatic effects, and $\frac{d}{dz}$ represents the rate at which a quantity changes as a parcel changes its vertical position.

We simplify this equation by making a series of approximations. First, we replace the moist heat capacity c_{pm} with the constant dry-air heat capacity c_{pd} and replace the temperature-dependent latent heat of vaporization with its reference value at the triple point temperature $L_{v,r}$, following numerous previous theoretical studies (e.g., Riehl and Malkus 1958; Romps 2014) and numerical model configurations (e.g., Khairoutdinov and Randall 2003). Second, we approximate $\frac{1}{\rho}\frac{dp}{dz} = -g$ using hydrostatic balance, where g is the acceleration of gravity. Note that this does not mean that we completely disallow nonhydrostatic vertical pressure gradient accelerations. Rather, we are neglecting the change in static energy with height resulting from work done by the parcel that is not directly exchangeable with gravitational potential energy (see Peters and Chavas 2021). Third, we temporarily neglect ice ($q_i = 0$), though the affects of ice will be accounted for later. Fourth, we assume that the only diabatic effect is the mixing of a parcel with its far-field environmental

[4]Mass fraction is defined as the ratio of the mass of a water variable (i.e., gas, liquid, solid) to the total air mass.

Accepted for publication in *Journal of the Atmospheric Sciences*. DOI 10.1175/JAS-D-23-0003.1.

profile. Using these approximations, we may re-write eq. 7 as:

$$\frac{dh}{dz} = -\varepsilon\left(h - h_0\right), \tag{8}$$

where h is the moist static energy, defined as

$$h = c_{pd}T + L_{v,r}q + gz, \tag{9}$$

h_0 is the moist static energy of the background environment, defined as:

$$h_0 = c_{pd}T_0 + L_{v,r}q_0 + gz, \tag{10}$$

the subscripts 0 denote the height-dependent background environmental profile, and we have dropped the v subscript on q for simplicity. The $-\varepsilon\left(h - h_0\right)$ term represents dilution of h with height due to entrainment, and is expressed in a manner consistent with a classical plume updraft model (e.g., Betts 1975). Note that for an adiabatic parcel (i.e., $\varepsilon \to 0$), h is conserved. Hence, h is analogous to equivalent potential temperature (θ_e). It will also be useful later to define the saturated moist static energy of the environment h_0^* as:

$$h_0^* = c_{pd}T_0 + L_{v,r}q_0^* + gz, \tag{11}$$

where q^* is the saturation mass fraction defined via eq. 10 in Bolton (1980). Finally, we define the buoyancy B of an updraft air parcel as:

$$B = g\frac{T - T_0}{T_0}, \tag{12}$$

which (temporarily) neglects the effects of water vapor and condensate loading on buoyancy. We will re-incorporate water vapor and condensate loading effects on buoyancy later on.

To evaluate the accuracy of these approximate equations, we integrate eq. 8 upward using a forward Euler integration scheme with a vertical grid spacing[5] of 100 m, and solve for T at each height using a the Matlab function "fsolve", a numerical nonlinear equation solver. We use

[5]This vertical grid spacing is sufficient to produce accurate buoyancy profiles, as is shown Fig. 11 in Peters et al. (2022c)

Accepted for publication in *Journal of the Atmospheric Sciences*. DOI 10.1175/JAS-D-23-0003.1.

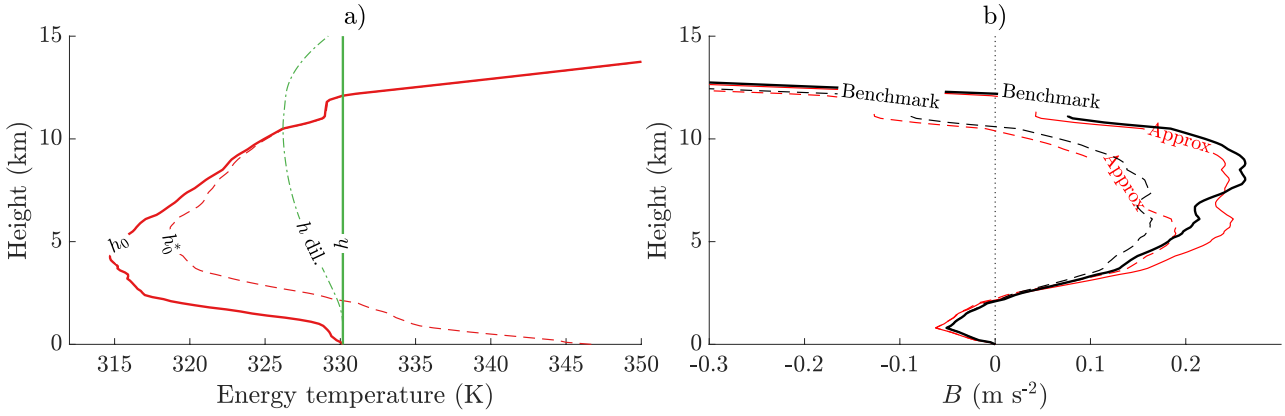

FIG. 1. Panel a: profiles of environmental h_0, h_0^*, and h of an undiluted parcel, and the h of a diluted parcel with $\varepsilon = 1 \times 10^{-4}$ m^{-1} ("h dil."), computed using the tornadic supercell composite profile from Parker (2014) as an example. Moist static energies have been divided by c_{pd} to yield "energy temperature" with units of K. Panel b: buoyancy of the diluted (dashed lines) and undiluted (solid lines) parcels, computed using the benchmark parcel (black, described in the beginning of section 2b) and from the approximate formula for h calculated by numerically integrating eq.8 as described in the text (red).

$\frac{dq}{dz} = -\varepsilon (q - q_0)$ during the unsaturated part of parcel ascent, and set $q = q^*$ during the saturated part of parcel ascent. Quantities such as buoyancy and ECAPE computed with eqs. 8 and 12 are referred to as "approximate". The vertical distributions of h_0 and h_0^* in a deep convective environment are shown in Fig. 1a. Much like the typical vertical distribution of θ_e, h has a local maximum in the lower troposphere when nonzero CAPE is present, a local minimum in the middle troposphere, and becomes large again in the lower stratosphere. An undiluted parcel lifted from the surface has larger h than its surroundings until it reaches the lower stratosphere. In an entraining parcel, h gradually relaxes to that of the background environment as the parcel ascends. Profiles of approximate buoyancy are compared to benchmark buoyancy, calculated from equations in Peters et al. (2022c) as described earlier in this section, for undiluted and diluted parcels in Fig. 1b. Despite the assumptions made thus far, the approximate and benchmark buoyancy profiles are comparable, having similar profile shapes and magnitudes at all heights.

Accepted for publication in *Journal of the Atmospheric Sciences*. DOI 10.1175/JAS-D-23-0003.1.

Our next task is to combining eqs. 9-11 to obtain an expression for B as a function of moist static energy variables, which yields:

$$B = \frac{g}{c_{pd}T_0}\left(h - h_0^*\right) - \frac{gL_{v,r}}{c_{pd}T_0}\left(q^* - q_0^*\right), \tag{13}$$

where we have assumed that the updraft parcel is saturated, such that $q = q^*$. The second term on the RHS of eq. 13 is often small relative to the first (e.g., Ahmed and Neelin 2018). Hence, eq. 13 suggests that $B > 0$ when $h > h_0^*$. This agrees with Fig. 1a-b, which shows approximate coincidence between the vertical extent of $h > h_0^*$ (Fig. 1a) and the vertical extent of $B > 0$ (Fig. 1b). An entrainment term (i.e., ε) does not show up explicitly in eq. 13, but is included implicitly via the moist static energy of the updraft parcel h, which is affected by entrainment. To make ε show up explicitly, we find the particular solution to eq. 8 with $h = h_0$ at $z = 0$, which may be written as:

$$h = e^{-\varepsilon z}\left(h_{ud} + \int_{\xi=0}^{\xi=z} \varepsilon e^{\varepsilon\xi} h_0 d\xi\right), \tag{14}$$

where h_{ud} is the moist static energy of an undiluted parcel, ξ is a dummy variable of integration, and we defined the parcel starting height as $z = 0$ for simplicity. Combining eq. 14 with eq. 13 yields the following:

$$B = \frac{g}{c_{pd}T_0}\left[e^{-\varepsilon z}\left(h_{ud} + \int_{\xi=0}^{\xi=z} \varepsilon e^{\varepsilon\xi} h_0 d\xi\right) - h_0^*\right] - \frac{gL_{v,r}}{c_{pd}T_0}\left(q^* - q_0^*\right). \tag{15}$$

The term ε now shows up explicitly in the equation, but is contained within an integral. We will need to make some additional approximations to bring this term out of the integrals to obtain our desired analytic solution.

Eq. 15 can be re-arranged to express B as a modification to the undiluted buoyancy B_{ud} using eq. 13 evaluated with $h = h_{ud}$ and $q = q_{ud}$:

$$\begin{aligned} B = B_{ud}e^{-\varepsilon z} + \frac{g}{c_{pd}T_0}\left(e^{-\varepsilon z}\int_{\xi=0}^{\xi=z} \varepsilon e^{\varepsilon\xi} h_0 d\xi - \left(1 - e^{-\varepsilon z}\right) h_0^*\right) \\ - \frac{gL_{v,r}}{c_{pd}T_0}\left(q^* - q_0^*\right) + e^{-\varepsilon z}\frac{gL_{v,r}}{c_{pd}T_0}\left(q_{ud}^* - q_0^*\right). \end{aligned} \tag{16}$$

Accepted for publication in *Journal of the Atmospheric Sciences*. DOI 10.1175/JAS-D-23-0003.1.

This re-arrangement allows us to use the traditional equation for buoyancy that includes hydrometeor loading and virtual temperature effects to compute B_{ud} (i.e., the black line in Fig. 1), rather than the approximate formula for buoyancy in eq. 12 which neglects the aforementioned effects (i.e., the red line in Fig. 1). This substitution generally improves the accuracy of the formula by re-introducing the virtual temperature and hydrometeor loading contributions to buoyancy that were neglected in eq. 12, and we use this approximation in all subsequent calculations.

We note that the last two terms on the RHS of eq. 16 will cancel each other in the limit of $\varepsilon \to 0$. In the opposite limit of $\varepsilon \to \infty$, each of these terms individual vanish because $q^* \to q_0^*$ and $e^{-\varepsilon z} \to 0$. We assume these terms are small in the intermediary range of ε, and consequently neglect them to simplify the equation. This approximation is further justified *a posteriori* later in this section via an error analysis. Using integration by parts and neglecting the aforementioned terms, we may re-write eq. 16 as:

$$B = B_{ud} e^{-\varepsilon z} + \frac{g}{c_{pd} T_0} \left(\varepsilon z \widehat{h_0} - e^{-\varepsilon z} \varepsilon^2 \int_{\xi=0}^{\xi=z} \widehat{h_0} \xi e^{\varepsilon \xi} d\xi - (1 - e^{-\varepsilon z}) \, h_0^* \right). \tag{17}$$

where $\widehat{h_0}(\xi) \equiv \frac{1}{\xi} \int_{\xi^*=0}^{\xi^*=\xi} h_0 d\xi^*$ is the average of h_0 below height ξ and $\widehat{h_0}$ in the first term in the parentheses on the RHS is evaluated at $\xi = z$. Assuming that $\widehat{h_0}$ is approximately constant with height allows us to bring this term out of the integral in eq. 17 and analytically evaluate the integral in the following manner:

$$-e^{-\varepsilon z} \varepsilon^2 \int_{\xi=0}^{\xi=z} \widehat{h_0} \xi e^{\varepsilon \xi} d\xi \approx -e^{-\varepsilon z} \varepsilon^2 \widehat{h_0} \int_{\xi=0}^{\xi=z} \xi e^{\varepsilon \xi} d\xi = -\varepsilon z \widehat{h_0} + (1 - e^{-\varepsilon z}) \, \widehat{h_0}. \tag{18}$$

This assumption dramatically simplifies eq. 17 to the following:

$$B = B_{ud} e^{-\varepsilon z} + \frac{g}{c_{pd} T_0} (1 - e^{-\varepsilon z}) \left(\widehat{h_0} - h_0^* \right). \tag{19}$$

We will provide an *a-posteriori* justification for this assumption shortly by evaluating the errors in profiles of B predicted from eq. 19 relative to the benchmark buoyancy calculation. Eq. 19 is an analytic function of B_{ud}, ε, and the state variables within a sounding. The first term on the RHS represents the direct dilution of the updraft's temperature perturbation via entrained air with

Accepted for publication in *Journal of the Atmospheric Sciences*. DOI 10.1175/JAS-D-23-0003.1.

no temperature perturbation, whereas the second term encapsulates the reduced condensation rate resulting from the entrainment of unsaturated air by the updraft, relative to an undiluted parcel.

Before moving on to an analytic formula for ECAPE, we evaluate the accuracy of this analytic buoyancy formula (and by extension justify the mathematical assumptions used to derive it) by comparing the average buoyancy $\overline{B}$ between the level of free convection (LFC) and the level of neutral buoyancy[6] (ELNB) to that of the benchmark buoyancy profile and the formula from P20 (eqs. 4-5 therein[7]). Here, the LFC is the highest instance of zero buoyancy below the height of maximum buoyancy, and the ELNB is the highest instance of zero buoyancy in the profile. We define two metrics for evaluation: Pearson correlation coefficient (CC) among soundings of $\overline{B}$ from eq. 19 with $\overline{B}$ from the more accurate benchmark lapse rate formula, and normalized root-mean-square-error (NRMSE) defined as the the average over all soundings of the squared difference between $\overline{B}$ from eq. 19 and $\overline{B}$ from the benchmark lapse rate formula, divided by the magnitude of $\overline{B}$ from the benchmark formula. These metrics, along with the fractional reduction in undiluted $\overline{B}$ by entrainment, are plotted as a function of ε and updraft radius R on the x axis. We relate R to ε using eq. 6, with $k^2 = 0.18$ (e.g., Morrison et al. 2022), $P_r = \frac{1}{3}$ (e.g., Deardorff 1972), and $L_{mix} = 120$ m following Morrison et al. (2022).

The CC of the new formula with the benchmark calculation is very close to 1 (Fig. 2a) for all $R > 750$ m and for fractional reductions in CAPE of < 0.9 (i.e., updrafts that realize 10 % or more of their CAPE; Fig. 2c), which is the range of fractional reductions expected in midlatitude deep convection (e.g., Peters et al. 2020b; Lasher-Trapp et al. 2021). For R less than 750 m and when fractional reductions approach 1, CC begins to drop, suggesting that the formula is less accurate for strongly entraining weak convection. The story is similar for NRMSE (Fig. 2e), which is relatively small in magnitude (i.e. < 0.1) for $R > 750$ m, but increases when R falls below 750 m. Compared to the P20 formula, the new formula derived here has smaller NRMSE Fig. 2e) and larger CC Fig. 2a), indicating that we have made an improvement in accuracy in the present derivation. This improvement over the P20 formula is primarily due to an over-estimation of the fractional reduction in buoyancy via entrainment in the P20 formula that does not occur in the one derived here (Fig. 2c), potentially due to the less accurate R^{-1} scaling with entrainment used in that study. This difference is particularly noticeable when we restrict our analysis to soundings

[6]The E in ELNB stand for "entraining", and differentiates this quantity from the traditional definition of the LNB that pertains to an undiluted parcel.

[7]We also use the B_{ud} computed with the benchmark parcel in the P20 formula to maximize this formula's accuracy.

Accepted for publication in *Journal of the Atmospheric Sciences*. DOI 10.1175/JAS-D-23-0003.1.

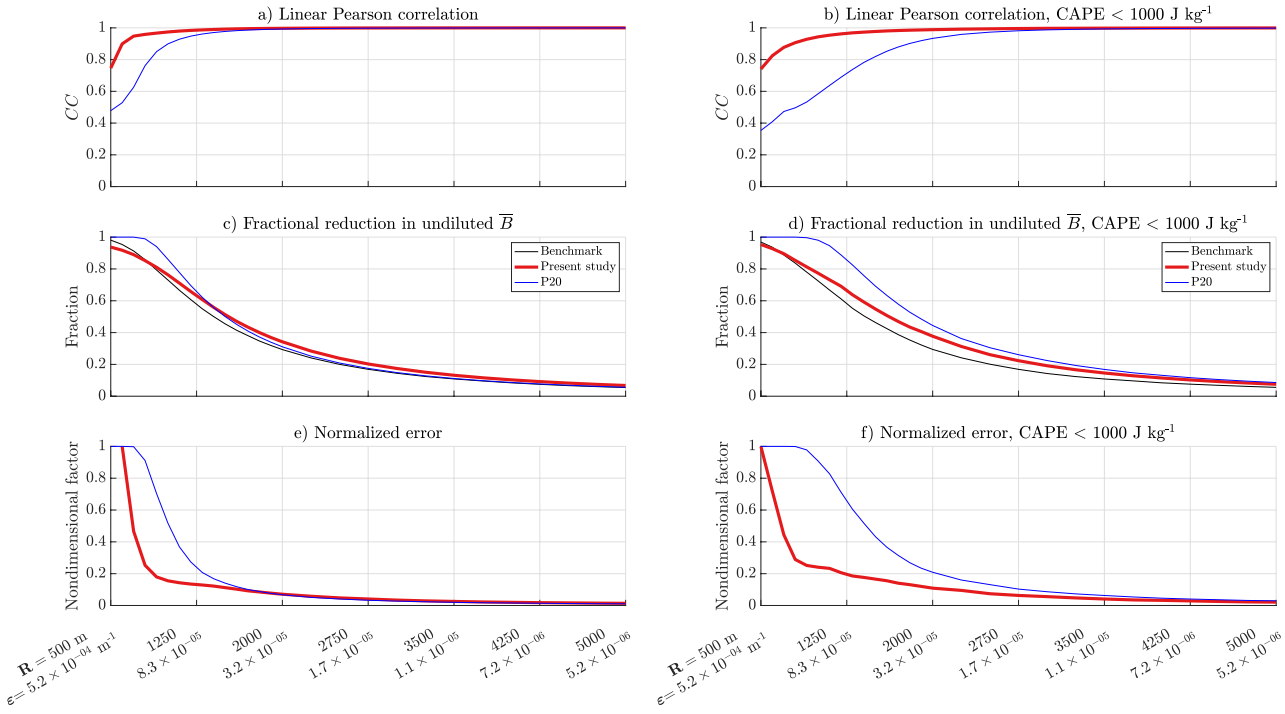

FIG. 2. Comparison of vertically-averaged buoyancy $\overline{B}$ calculated using the formula from the present study (eq. 19, red), the P20 buoyancy formula (gray), and the benchmark parcel (black). Panels a,b show CC, c,d the fractional reduction in $\overline{B}$, and e,f the NRMSE. CC and NRMSE are calculated relative to the benchmark parcel. Left panels show results from all Thompson et al. (2003) soundings, and right panels show results from only soundings with < 1000 J kg^{-1} undiluted CAPE to illustrate the shortcomings of the P20 formula.

with less than 1000 J kg^{-1} of undiluted CAPE (Fig. 2b,d,f). In this low CAPE regime, the NRMSE (Fig. 2f) and CC (Fig. 2b) of the new formula are comparable to the errors for the whole sounding data set, whereas the P20 formula performs considerably worse with respect to both CC and errors in the low CAPE regime.

Our next task is to use eq. 19 to obtain an expression for ECAPE. We define ECAPE as:

$$\text{ECAPE} = \int_{z=LFC}^{z=ELNB} B dz. \tag{20}$$

Vertically integrating eq. 19 from the LFC to the ELNB and combining with eq. 20 yields:

$$\text{ECAPE} = \int_{z=LFC}^{z=ELNB} B_{ud} e^{-\varepsilon z} dz + \int_{z=LFC}^{z=ELNB} \frac{g}{c_{pd} T_0} (1 - e^{-\varepsilon z}) \left(\widehat{h_0} - h_0^* \right) dz. \tag{21}$$

Accepted for publication in *Journal of the Atmospheric Sciences*. DOI 10.1175/JAS-D-23-0003.1.

It will make it easier to pull ε out of the integral terms if we have the integral bounds on the RHS of eq. 21 extend to the LNB for an undiluted parcel[8] H, rather than to the ELNB. We note that the integral of the first term from the ELNB to the H will always be positive, since B_{ud} is positive below the H by definition. On the other hand, the integral of the second term over this range is typically negative (as will be discussed shortly), and at least partially cancels the contribution of the integral of the first term over this range. Hence, we extend the upper bounds of these integrals to the H, assuming that the partial cancellation between the terms mitigates the resulting errors. This assumption is evaluated *a-posteriori* later in this section using an error analysis.

To pull ε out of the integrals in eq. 21, we use integration by parts and these integral definitions to write the first term on the RHS of eq. 21 as:

$$\int_{z=LFC}^{z=H} B_{ud} e^{-\varepsilon z} dz = e^{-\varepsilon H}\text{CAPE} + \varepsilon \int_{z=LFC}^{z=H} e^{-\varepsilon z} (z - LFC) \widehat{B_{ud}} dz \tag{22}$$

where

$$\text{CAPE} = \int_{z=LFC}^{z=H} B_{ud} dz, \tag{23}$$

and

$$\widehat{B_{ud}} = \frac{1}{z - LFC} \int_{\xi=LFC}^{\xi=z} B_{ud} d\xi, \tag{24}$$

Following the steps taken in eq. 18, we assume that $\widehat{B_{ud}}$ is constant with height and pull this term out of the integral in eq. 22, which allows us to analytically evaluate the integral. We also assume that $LFC << H$ and hence $H - LFC \approx H$, and neglect entrainment below the LFC such that $e^{-\varepsilon LFC} \approx 1$. We apply analogous assumptions to the 2nd term on the RHS of eq. 21. Once again, these assumptions are justified *a posteriori* via an error analysis later in this section. Modifying eq. 21 with these assumptions yields:

$$\text{ECAPE} = \left(\frac{1 - e^{-\varepsilon H}}{\varepsilon H}\right)\text{CAPE} - \left(1 - \frac{1 - e^{-\varepsilon H}}{\varepsilon H}\right)\text{NCAPE} \tag{25}$$

where

$$\text{NCAPE} = -\int_{z=LFC}^{z=H} \frac{g}{c_{pd} T_0} \left(\widehat{h_0} - h_0^*\right) dz, \tag{26}$$

[8] We use the symbol H in equations for compactness to represent the LNB for compactness.

Accepted for publication in *Journal of the Atmospheric Sciences*. DOI 10.1175/JAS-D-23-0003.1.

where the N in NCAPE stands for "negative." The coefficient $\left(\frac{1-e^{-\varepsilon H}}{\varepsilon H}\right)$ ranges from 0 to 1, with small and large values reflecting strong and weak entrainment-driven dilution respectively.

There are several parallels between eq. 25 and the analytic-empirical formula for buoyancy derived by Ahmed and Neelin (2018) to explain the physical processes responsible for the relationship between plume buoyancy and precipitation in the tropics. Physically, the first term on the RHS of eq. 25 represents the dilution of CAPE via the entrainment of air outside the updraft with zero buoyancy, and is analogous to the saturation terms derived in section 3c of Ahmed and Neelin (2018). NCAPE represents the potential buoyancy loss from the entrainment of dry air into the updraft and the associated reduction in the condensation and deposition rate, and is analogous to the saturation deficit terms in section 3c of Ahmed and Neelin (2018). NCAPE is purely dependent on environmental variables (like CAPE), and is principally determined by the saturation deficit of the environment. The definition of $\widehat{h_0}$ as an average below a given level captures the cumulative effect of entrainment with height. Because h_0^* is comparable to or larger than $\widehat{h_0}$ (Fig. 3a), NCAPE is typically positive (Fig. 3b). In (rare) conditions where the free troposphere is very moist, NCAPE becomes negative. This is an unphysical artifact of our assumption that the water vapor mixing ratio in the updraft is equal to the saturation water vapor mixing ratio of the surrounding environment, and we simply set NCAPE to zero in these situations.

The difference term in the integral $\widehat{h_0} - h_0^*$ (Fig. 3a) and hence the magnitude of NCAPE (Fig. 3b) will be larger when the free troposphere is dry and $\widehat{h_0}$ is far smaller than h_0^*, compared to when the free troposphere is moist and $\widehat{h_0}$ is closer in magnitude to h_0^*. A warm free troposphere at a given RH generally increases the difference between h_0^* and $\widehat{h_0}$ (Fig. 3c) compared to a situation when the free troposphere is cool at the same RH. For a fixed RH, this makes NCAPE larger when the free troposphere is warm, relative to when it is cool (Fig. 3d). Hence, NCAPE generally encapsulates the effects of tropospheric dryness and temperature on buoyancy via entrainment.

Eq. 25 achieves the stated purpose of this derivation, since ε is now outside of the integral terms. It will become advantageous in the next sub-section to further simplify the exponential terms in eq. 25. One may consider making first order Taylor series approximations for the exponential terms. For instance $\frac{1-e^{-\varepsilon H}}{\varepsilon H} \approx 1 - \frac{\varepsilon H}{2}$. However, the exponential functions in eq. 25 are strongly nonlinear with respect to εH in the range of $0 < \varepsilon H < 10$, which is the typical range we would encounter in our analysis, making the first order Taylor series approximation inaccurate (compare the blue and

Accepted for publication in *Journal of the Atmospheric Sciences*. DOI 10.1175/JAS-D-23-0003.1.

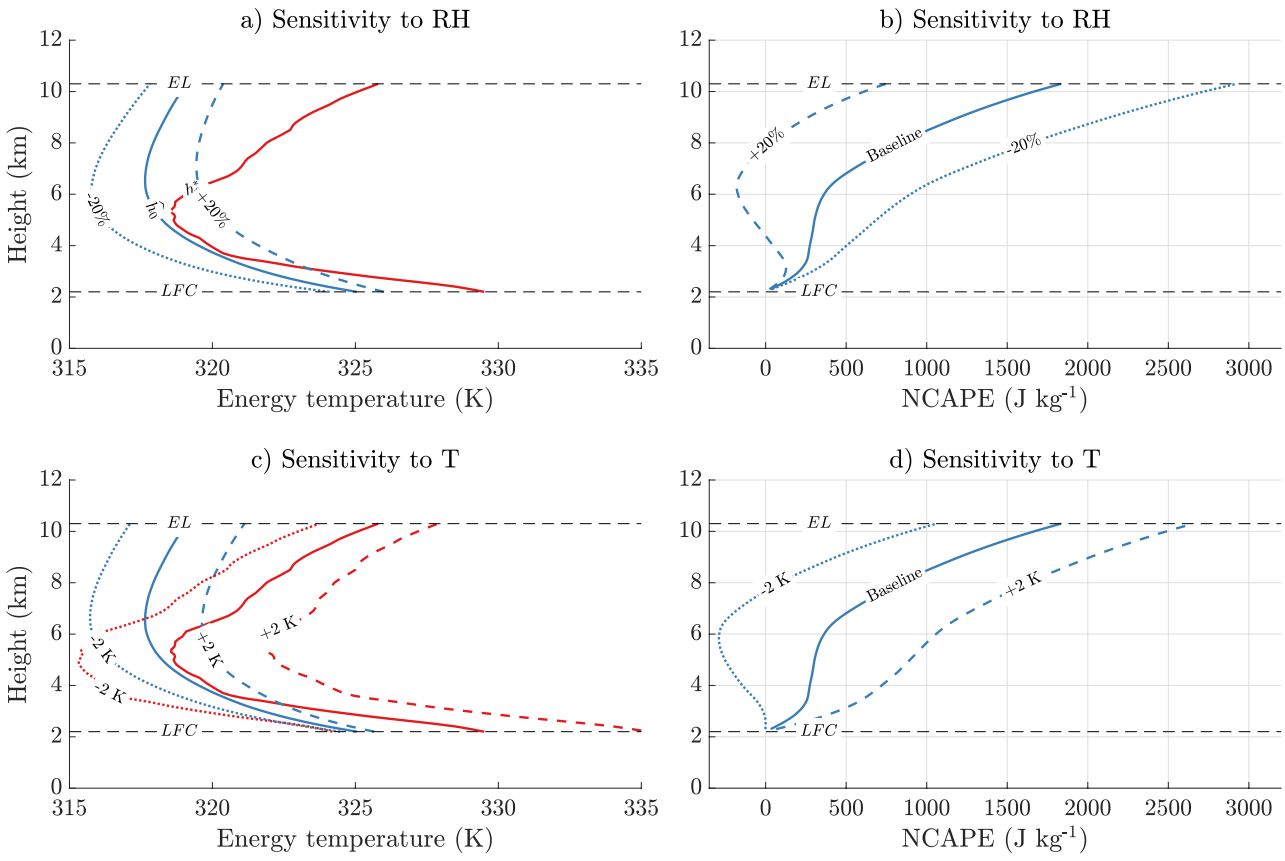

FIG. 3. Demonstrations of the sensitivities of NCAPE to relative humidity (RH) and free tropospheric temperature. Panel a: profiles of h_0^* (red, divided by c_{pd} to yield units of K), and $\widehat{h}_0$ (blue, K) for the baseline sounding (solid), RH increased by 20 % (dashed blue), and RH decreased by 20 % (dotted blue). Panel b: profiles of NCAPE (J kg^{-1}) corresponding to panel a. Panels c-d: analogous to panels a-b, but showing differences in h_0^* and $\widehat{h}_0$ resulting from an increase in T by 2 K with RH held constant (dashed), and a decrease in T of 2 K with RH held constant (dotted).

black lines in Fig. 4a). Instead, we invert the exponential term $\frac{1-e^{-\varepsilon H}}{\varepsilon H}$, approximate its inverse with a first order Taylor series, and then invert the result. For instance:

$$\frac{\varepsilon H}{1-e^{\varepsilon H}} \approx 1+\frac{\varepsilon H}{2}. \tag{27}$$

and consequently:

$$\frac{1-e^{\varepsilon H}}{\varepsilon H} \approx \frac{1}{1+\frac{\varepsilon H}{2}}. \tag{28}$$

Accepted for publication in *Journal of the Atmospheric Sciences*. DOI 10.1175/JAS-D-23-0003.1.

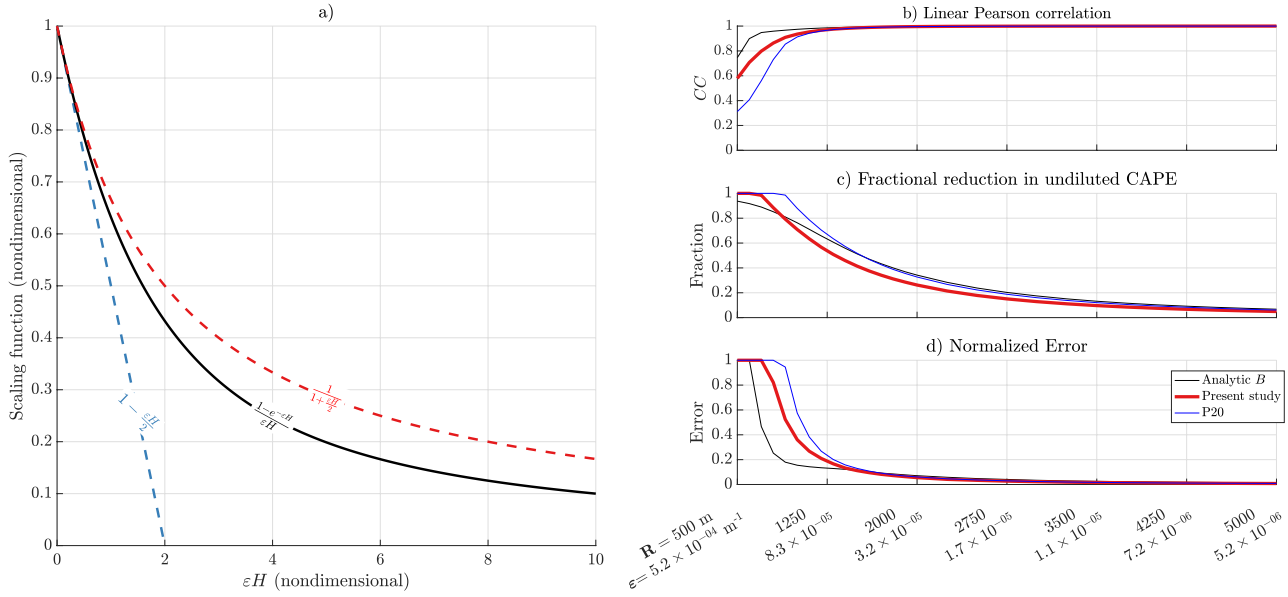

FIG. 4. Panel a: comparison of the scale factor in eq. 25 (solid black) with its first order Taylor series approximation (blue dashed), and the first order Taylor series approximation of its inverse (dashed red). Panels b-d: analogous to Fig. 2a,b,c, but evaluating ECAPE from eq. 29 (red, the present article), ECAPE from P20 (gray), and ECAPE from numerically integrating eq. 19 (black), all relative to the benchmark calculation.

This approximation is far more accurate (compare the red and black lines in Fig. 4a). Substituting these approximations into eq. 25 and re-arranging yields:

$$\text{ECAPE} = \frac{\text{CAPE} - \frac{\varepsilon H}{2}\text{NCAPE}}{1 + \frac{\varepsilon H}{2}}. \tag{29}$$

As a sanity check, we examine the behavior of eq. 29 under limiting scenarios. For instance, in the limit of no entrainment where $\varepsilon \to 0$, ECAPE $\to$ CAPE, which makes sense given that ECAPE for an undiluted parcel intuitively converges to the CAPE. In the converse limit of $\varepsilon \to \infty$, we may use L'Hôpital's rule to deduce that ECAPE $\to -$NCAPE, which is inconsistent with the definition of CAPE as a quantity greater than or equal to zero. However, this situation is easily remedied by simply setting ECAPE to a minimum value of 0.

The analytic formula for ECAPE in eq. 29 loses a bit of accuracy relative to the numerically integrated analytic buoyancy equation at larger values of ε (i.e., smaller updraft radii; Fig. 4b-d), but remains more accurate than the formula for maximum updraft vertical velocity w_{max} from P20

Accepted for publication in *Journal of the Atmospheric Sciences*. DOI 10.1175/JAS-D-23-0003.1.

(Eq. 18 therein, which is converted to ECAPE via $\frac{w_{max}^2}{2}$), with the main improvement over that formula occurring for narrow updrafts. These errors stem from a slight underestimation of the fractional reduction in undiluted CAPE at large ε values (Fig. 4c) that results from our changing of the integral bounds in eq. 21 from the LNB to H. Despite these errors, this formula is quite accurate over the range of R and ε that typify deep moist convection (i.e., fractional reductions of no greater than 0.8, Fig. 4c).

e. Relating fractional entrainment to environmental variables

To make formulas more compact and easier to algebraically manipulate in subsequent steps, we convert them to nondimensional forms. We define the nondimensional ECAPE as $\widetilde{E} \equiv \frac{\text{ECAPE}}{\text{CAPE}}$, the nondimensional NCAPE as $\widetilde{N} \equiv \frac{\text{NCAPE}}{\text{CAPE}}$, and the nondimensional fractional entrainment rate $\widetilde{\varepsilon} \equiv \varepsilon H$. Using these definitions, we re-write eq. 29 as:

$$\widetilde{E} = \frac{1 - \frac{\widetilde{\varepsilon}}{2}\widetilde{N}}{1 + \frac{\widetilde{\varepsilon}}{2}}. \tag{30}$$

Our next task is to eliminate $\widetilde{\varepsilon}$ from eq. 29 by expressing this term as function of other updraft and environmental attributes. We proceed by defining $\widetilde{R} \equiv \frac{R}{H}$ and use eq. 6 to write:

$$\widetilde{\varepsilon} = \epsilon \widetilde{R}^{-2}, \tag{31}$$

where

$$\epsilon = \frac{2k^2 L_{mix}}{HP_r}. \tag{32}$$

Combining eq. 31 with eq. 30 yields:

$$\widetilde{E} = \frac{1 - \frac{\epsilon}{2\widetilde{R}^2}\widetilde{N}}{1 + \frac{\epsilon}{2\widetilde{R}^2}}. \tag{33}$$

Following P20 and Peters et al. (2022a), we may express $\widetilde{R}$ as a function of updraft and environmental attributes by making the following assumptions about updraft geometry and inflow:

1. Updrafts are cylindrical.

Accepted for publication in *Journal of the Atmospheric Sciences*. DOI 10.1175/JAS-D-23-0003.1.

2. R (and consequently $\widetilde{R}$) are constant with height. Numerous previous studies show this to be approximately valid (e.g., Sherwood et al. 2013; Hernandez-Deckers and Sherwood 2016; Morrison et al. 2021).

3. We assume that all environmental storm-relative wind $\mathbf{V}_{SR}$ that encounters the cross-sectional area of the updraft on the upstream side becomes inflow. Past studies also show this assumption to be reasonable (e.g., Peters et al. 2019, 2022b).

4. The updraft maximum vertical velocity w_{max} is proportional to the horizontally averaged vertical velocity $< w >$ at the same height, such that $< w >= \alpha w_{max}$, where $0 < \alpha < 1$ (e.g., Morrison 2017; Morrison and Peters 2018).

5. For the time being, we assume that the updraft maximum vertical velocity is primarily determined by updraft buoyancy, such that $w_{max} = \sqrt{2\text{ECAPE}}$. This assumption is supported by previous studies (Morrison and Peters 2018; Jeevanjee 2017; Peters et al. 2019, 2020a). We will relax this assumption later on.

6. w_{max} occurs at height H, which follows from assumption 5.

With these assumptions at hand, we start by writing the anelastic continuity equation in cylindrical coordinates as:

$$\rho_0 \frac{\partial ru}{\partial r} + \rho_0 \frac{\partial v}{\partial \phi} + r \frac{\partial \rho_0 w}{\partial z} = 0. \tag{34}$$

Azimuthally integrating from $\phi = 0$ to $\phi = 2\pi$, radially integrating from $r = 0$ to the updraft radius at $r = R$, and vertically integrating from the surface to H (assuming $w = 0$ at $z = 0$) and dividing by 2π yields:

$$H\widehat{\rho_0}\widehat{u}_R + R\frac{\rho_{0,H} < w_H >}{2} = 0. \tag{35}$$

where

$$\widehat{u}_R = \frac{1}{2\pi} \frac{\int_{z=0}^{z=H} \rho_0 \int_{\phi=0}^{\phi=2\pi} u d\phi dz}{\int_{z=0}^{z=H} \rho_0 dz} \tag{36}$$

is the density-weighted vertical average of u at radius R, and between the surface and height H, and represents the average inflow speed,

$$< w >= \frac{1}{\pi R^2} \int_{r=0}^{r=R} \int_{\phi=0}^{\phi=2\pi} r w d\phi dr \tag{37}$$

Accepted for publication in *Journal of the Atmospheric Sciences*. DOI 10.1175/JAS-D-23-0003.1.

is the area average of w within radius R, $\widehat{\rho_0}$ is the vertical average of ρ_0 between the surface and height H, and $\rho_{0,H}$ is ρ_0 valid at height H. Making use of $< w >= \alpha w_{max}$ (assumption 4) at height H and $\frac{w_{max}^2}{2} = ECAPE$ (assumption 5), and re-arranging eq. 35 yields:

$$\widetilde{R} = -2\frac{\sigma}{\alpha}\frac{\widehat{u}_R}{\sqrt{2\text{ECAPE}}}, \tag{38}$$

where $\sigma = \frac{\widehat{\rho_0}}{\rho_{0,H}} > 1$. We may relate $\widehat{u}_R$ to the horizontal storm-relative wind speed $V_{SR} = |\mathbf{V}_{SR}|$, where $\mathbf{V}_{SR}$ is the storm-relative wind vector, by first defining the upstream flank of the updraft as the range from $\phi = -\frac{\pi}{2}$ to $\phi = \frac{\pi}{2}$. We next assume that all inflow is accomplished by the cloud-relative wind entering the upstream updraft flank, and the radial component of the environmental cloud-relative wind at the updraft edge is $u = -V_{SR}\cos\phi$ and $u = 0$ m s^{-1} on the downstream edge. The aforementioned assumptions allow us to re-write eq. 36 as:

$$\widehat{u}_R = -\frac{1}{2\pi}\frac{\int_{z=0}^{z=H}\int_{\phi=-\frac{\pi}{2}}^{\phi=\frac{\pi}{2}}\rho_0 V_{SR}\cos\phi d\phi dz}{\int_{z=0}^{z=H}\rho_0 dz} = -\frac{\widehat{V_{SR}}}{\pi}, \tag{39}$$

where $\widehat{V_{SR}}$ is the density weighted vertical average of V_{SR} below height H. Physically, these assumptions imply that the entirety of storm-relative flow below the height of w_{max} is absorbed by the updraft. In other words, all storm-relative flow becomes inflow. There is support for this behavior in past simulations. For instance, Fig. 4 in Peters et al. (2019) shows that storm-relative flow below 3 km strongly correlates with inflow in that layer, and Figs. 11a and 15a-b in Peters et al. (2022b) show that the horizontal storm-relative flow component nearly vanishes on the downstream of flank of simulated updrafts at low-levels. The assumption of all inflow being absorbed is more tenuous aloft near the height of w_{max}. However, winds aloft contribute far less to the vertical average in $\widehat{V_{Sr}}$ than winds at lower levels because of the density weighting in eq. 39.

In defining $\widetilde{v} \equiv \frac{\widehat{V_{SR}}}{\sqrt{2\text{CAPE}}}$, combining eqs. 38 and 39 and the definition of ϵ, and squaring and inverting the result, we obtain

$$\widetilde{R}^{-2} = \frac{\alpha^2\pi^2}{4\sigma^2}\frac{\widetilde{E}}{\widetilde{v}^2}. \tag{40}$$

Accepted for publication in *Journal of the Atmospheric Sciences*. DOI 10.1175/JAS-D-23-0003.1.

combining eq. 40 with eq. 33 (our expression for $\widetilde{E}$ as a function of $\widetilde{R}$) to eliminate $\widetilde{R}$ yields:

$$\widetilde{E}^2 \frac{\psi}{\widetilde{v}^2} + \widetilde{E}\left(1 + \frac{\psi}{\widetilde{v}^2}\widetilde{N}\right) - 1 = 0, \tag{41}$$

where

$$\psi = \frac{k^2 \alpha^2 \pi^2 L_{mix}}{4 P_r \sigma^2 H}, \tag{42}$$

and $\widetilde{E}$ is the only remaining unknown that is not computed from constants or the background sounding. Solving eq. 41 for $\widetilde{E}$ using the quadratic formula gives:

$$\widetilde{E} = \frac{-1 - \frac{\psi}{\widetilde{v}^2}\widetilde{N} + \sqrt{\left(1 + \frac{\psi}{\widetilde{v}^2}\widetilde{N}\right)^2 + 4\frac{\psi}{\widetilde{v}^2}}}{2\frac{\psi}{\widetilde{v}^2}}, \tag{43}$$

where we have neglected the negative quadratic root that yields an imaginary solution. Solutions for $\widetilde{E}$, which represent the fractional reduction of undiluted CAPE by entrainment, are contoured in Fig. 5a as a function of $\widetilde{v}$ (non-dimensional storm-relative flow speed) and $\widetilde{N}$ (non-dimensional NCAPE). In general, $\widetilde{E}$ increases from left-to-right in the figure as $\widetilde{v}$ becomes large, indicating stronger storm-relative inflow, wider updrafts, and hence smaller fractional entrainment. From bottom-to-top on the figure, $\widetilde{E}$ decreases as $\widetilde{N}$ increases. This trend occurs because larger $\widetilde{N}$ implies a drier and/or warmer mean free troposphere, both of which amplify entrainment-driven dilution relative to situations with a cooler and/or moister free troposphere.

In dimensional form, eq 43 is:

$$\text{ECAPE} = \frac{-1 - \frac{2\psi}{V_{SR}^2}\text{NCAPE} + \sqrt{\left(1 + \frac{2\psi}{V_{SR}^2}\text{NCAPE}\right)^2 + \frac{8\psi}{V_{SR}^2}\text{CAPE}}}{4\frac{\psi}{V_{SR}^2}}. \tag{44}$$

Solutions for ECAPE from eq. 44 as a function of V_{SR} and CAPE are shown in Fig. 5b,c,d for NCAPE=500 J kg^{-1}, 1000 J kg^{-1}, and 5000 J kg^{-1} respectively. In general, curves of ECAPE take on hyperbolic shapes with respect to the x and y axes, with contours of ECAPE paralleling the x axis for large V_{SR}, and the y axis for small V_{SR} and large CAPE, and with the largest values coinciding with the largest V_{SR} and undiluted CAPE in the upper-right corners of the figures. This pattern

Accepted for publication in *Journal of the Atmospheric Sciences*. DOI 10.1175/JAS-D-23-0003.1.

means that different combinations of V_{SR} and undiluted CAPE may result in similar ECAPE. For instance, an environment with 1000 J kg^{-1} of undiluted CAPE, a V_{SR} of 30 m s^{-1}, and an NCAPE of 5000 J kg^{-1}, has an ECAPE of roughly 1000 J kg^{-1} (Fig. 5d). Due to their large V_{SR}, mature isolated deep convective updrafts in this environment will be sufficiently wide to be approximately undiluted and thereby realize nearly all of their undiluted CAPE. A contrasting environment with 6000 J kg^{-1} of undiluted CAPE and an NCAPE of 5000 J kg^{-1}, but with a V_{SR} of only 5 m s^{-1} will have a similar ECAPE of 1000 J kg^{-1}. Despite the large undiluted CAPE in the second environment, updrafts are narrow and substantially diluted by entertainment because of small V_{SR}.

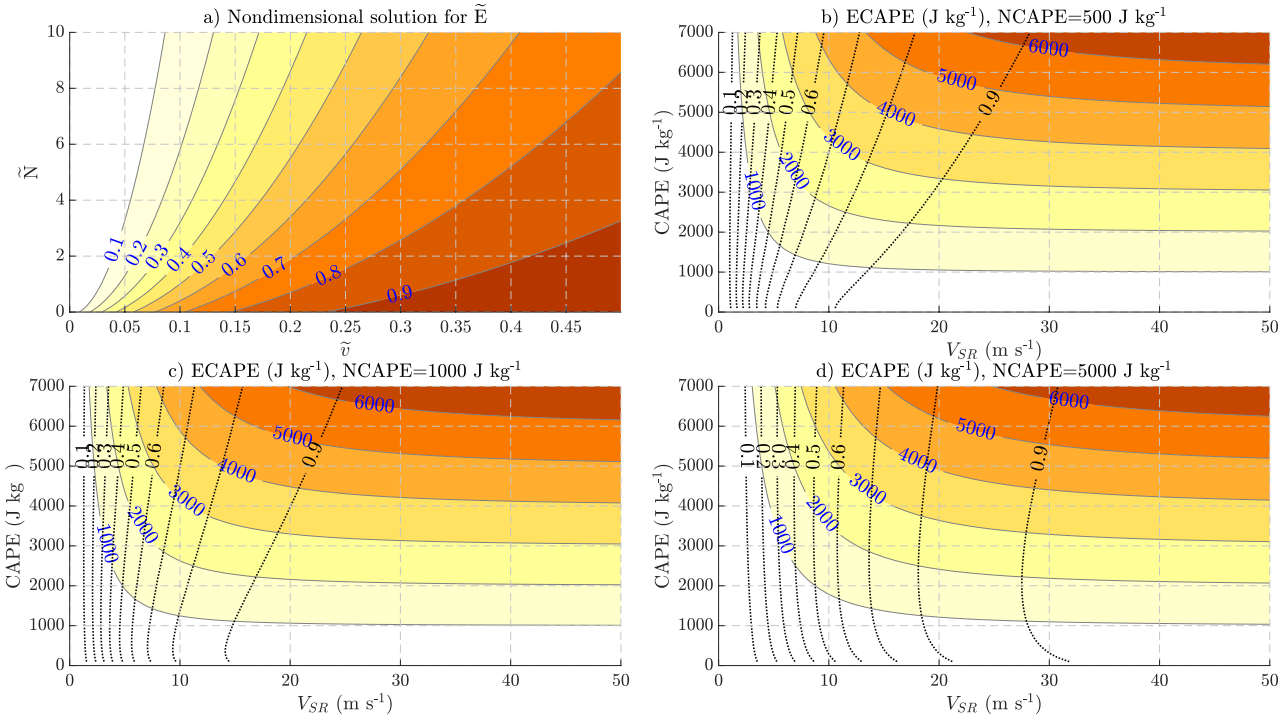

FIG. 5. Panel a: $\widetilde{E}$ (shading) as a function of $\widetilde{v}$ (x axis) and $\widetilde{N}$ (y axis), with H set to 12,000 m, L = 120 m, α = 0.8, σ = 1.131, k^2 = 0.18, and $P_r = \frac{1}{3}$. Panels b-d: ECAPE (shading, J kg^{-1}) as a function of V_{SR} (x axis, m s^{-1}) and undiluted CAPE (y axis, J kg^{-1}), and $\widetilde{E}$ (black contours), with NCAPE = 500 J kg^{-1} (panel a), NCAPE = 1000 J kg^{-1} (panel b), and NCAPE = 5000 J kg^{-1} (panel c). In panels b-d, H is determined via $H = 5808 + 96.12\sqrt{2CAPE}$, based on a linear regression between these variables among the soundings. All other parameters are the same as in panel a.

Consistent with the dependence of $\widetilde{E}$ on $\widetilde{N}$ seen in Fig. 5a, the fractional reduction in undiluted CAPE by ECAPE increases as NCAPE increases, particularly for smaller values of undiluted

Accepted for publication in *Journal of the Atmospheric Sciences*. DOI 10.1175/JAS-D-23-0003.1.

CAPE. This is most evident as a movement to the right of the contours of $\widetilde{E}$ (black) in Fig. 5b-d as NCAPE increases, indicating that an updraft with a given combination of undiluted CAPE and V_{SR} will realize less of its CAPE when NCAPE is large, compared to when NCAPE is small.

f. Accounting for kinetic energy the storm derives from its environment

While it is somewhat infrequent, past studies have documented instances in supercells where w_{max} exceeds $\sqrt{2\text{CAPE}}$ for extended periods of time (e.g., Fiedler 1994), likely due to vertical pressure gradient accelerations. This section introduces a simple adjustment factor to the ECAPE formula to represent of how such pressure effects redirect environmental kinetic energy into the updraft. To derive this adjustment factor, we must make the following assumptions:

1. The Lagrangian evolution of kinetic energy following an air parcel is well described by the Boussinesq approximation, meaning that ρ_0 is constant. Past studies have shown that errors related to an over-estimation of ρ_0 aloft in deep convective environments have a small effect on analytic solutions for vertical velocity, (e.g., Morrison 2016a,b).

2. Dynamic pressure perturbation acceleration (DPA) in the lower troposphere is assumed to deflect horizontal environmental kinetic energy into the vertical direction within the updraft.

3. DPA in the *middle-to-upper troposphere* is neglected. Dynamic pressure perturbations aloft may be large in magnitude, but they typically occur within the toroidal circulations of moist thermals (e.g., Romps and Charn 2015; Morrison and Peters 2018; Peters and Chavas 2021). As parcels ascend through these thermals, they experience an upward acceleration below the minimum in p', and then a commensurate downward acceleration above the minimum in p'. Hence, any temporary kinetic energy gained by the interaction of a parcel with these pressure perturbations is quickly lost.

4. Buoyancy pressure perturbation acceleration (BPA) is neglected, because there is evidence in past literature that the effect of BPA on overall updraft *maximum w* is small (Morrison and Peters 2018; Peters et al. 2019, 2020a), though we acknowledge that BPA may substantially alter the vertical distribution of vertical accelerations (e.g., Peters 2016; Kuo and Neelin 2022). In fact, it is possible to amend the formulas in this article to include buoyancy pressure perturbation accelerations, though this substantially increases the complexity of the resulting

Accepted for publication in *Journal of the Atmospheric Sciences*. DOI 10.1175/JAS-D-23-0003.1.

ECAPE formula. Repeating our analysis with this modification (not shown) affirmed that the influence of BPA on ECAPE does not substantially alter our results.

5. Direct dilution of kinetic energy via entrainment is negligible. This assumption is also supported by past studies (e.g., Sherwood et al. 2013). Note that entrainment will still indirectly affect kinetic energy via the entrainment-driven dilution of updraft buoyancy.

6. Updrafts are approximately steady, such that $\frac{\partial}{\partial t}$ of quantities are small.

7. The magnitude of convective inhibition (CIN) is negligable relative to the magnitude of ECAPE.

8. Horizontal storm-relative flow vanishes at the height of w_{max}.

We may use the first assumption to write eq. 15 in Peters and Chavas (2021), which describes the Lagrangian tendency for kinetic energy, as:

$$\frac{dKE}{dt} = \mathbf{V} \cdot \nabla \left(\frac{p'}{\rho_0} \right) + wB \tag{45}$$

where p' is a pressure perturbation. We define kinetic energy (KE) here in an updraft relative sense, such that $KE = \frac{u_{CR}^2 + v_{CR}^2 + w^2}{2}$, where u_{CR} and v_{CR} are the u and v cloud-relative wind components. Because of the steady state assumption, we may substitute $\frac{d}{dt}\left(\frac{p'}{\rho_0}\right) = \mathbf{V} \cdot \nabla \left(\frac{p'}{\rho_0} \right)$. We further use the chain rule to write $\frac{d}{dt} = w\frac{d}{dz}$, where $\frac{d}{dz}$ is the rate of change of a quantity as a parcel changes height. Making these assumptions and substitutions, and integrating from a parcel starting position (defined as $z = 0$) to an ending position at the height of w_{max} yields the following form of the classical Bernoulli equation:

$$KE_{LNB} - KE_0 = \frac{p'_{LNB}}{\rho} - \frac{p'_0}{\rho} + \int_{z=0}^{z=LNB} B dz. \tag{46}$$

If a parcel originates within an updraft's unmodified background environmental flow then $p' = 0$, $w = 0$, and $KE_0 = \frac{V_{SR}^2}{2}$. We may also neglect $\frac{p'_{LNB}}{\rho}$ because of assumption (2) above. Finally, we note that $\int_{z=0}^{z=LNB} B dz = \text{ECAPE} + \text{ECIN}$, where ECIN is the convective inhibition for an entraining parcel (ECAPE here is defined via eq. 44). Combining all these assumptions and substitutions, neglecting ECIN, and assuming that horizontal storm-relative flow vanishes at the height of w_{max}

Accepted for publication in *Journal of the Atmospheric Sciences*. DOI 10.1175/JAS-D-23-0003.1.

gives:

$$\text{ECAPE}_A = \frac{w_{max}^2}{2} = \frac{V_{SR}^2}{2} + \text{ECAPE} \tag{47}$$

where the subscript A indicates "adjusted". According to this equation, the role of low-level pressure perturbations is to preserve the incoming cloud-relative horizontal kinetic energy, deflecting it into the vertical. Further, the maximum updraft kinetic energy at the height of w_{max} consists of the sum of the kinetic energy gained from the release of ECAPE and the kinetic energy of the redirected inflow. Nondimensionalizing by the undiluted CAPE yields:

$$\widetilde{E}_A = \widetilde{v}^2 + \widetilde{E}, \tag{48}$$

where $\widetilde{E}_A$ is the nondimensional analogy to ECAPE_A. Recall that in the derivation in the previous sub-section, we neglected pressure effects and assumed that $\text{ECAPE} = \frac{w_{max}^2}{2}$ when deriving the expression for R^{-2} in eq. 40. Now we must account for the influence of the added contribution to w_{max} from velocity from environmental kinetic energy on updraft radius. Hence, we set $\text{ECAPE}_A = \frac{w_{max}^2}{2}$, and adjust eq. 40 using eq. 48 to:

$$\widetilde{R}^{-2} = \frac{\alpha^2\pi^2}{4\sigma^2}\frac{w_{max}^2}{V_{SR}^2} = \frac{\alpha^2\pi^2}{4\sigma^2}\left(\frac{\widetilde{E}}{\widetilde{v}^2} + 1\right). \tag{49}$$

Combining eqs. 48-49 with eq. 33 yields:

$$\widetilde{E}^2\frac{\psi}{\widetilde{v}^2} + \widetilde{E}\left(1 + \psi + \frac{\psi}{\widetilde{v}^2}\widetilde{N}\right) - 1 + \psi\widetilde{N} = 0, \tag{50}$$

Solving $\widetilde{E}$ using the quadratic formula and then plugging the result into eq. 48 to solve for $\widetilde{E}_A$ gives:

$$\widetilde{E}_A = \widetilde{v}^2 + \frac{-1 - \psi - \frac{\psi}{\widetilde{v}^2}\widetilde{N} + \sqrt{\left(1 + \psi + \frac{\psi}{\widetilde{v}^2}\widetilde{N}\right)^2 + 4\frac{\psi}{\widetilde{v}^2}\left(1 - \psi\widetilde{N}\right)}}{2\frac{\psi}{\widetilde{v}^2}}, \tag{51}$$

Accepted for publication in *Journal of the Atmospheric Sciences*. DOI 10.1175/JAS-D-23-0003.1.

which may be written dimensionally as:

$$\mathrm{ECAPE}_A = \frac{V_{SR}^2}{2} + \frac{-1-\psi-\frac{2\psi}{V_{SR}^2}\mathrm{NCAPE}+\sqrt{\left(1+\psi+\frac{2\psi}{V_{SR}^2}NCAPE\right)^2+8\frac{\psi}{V_{SR}^2}\left(\mathrm{CAPE}-\psi\mathrm{NCAPE}\right)}}{4\frac{\psi}{V_{SR}^2}}. \tag{52}$$

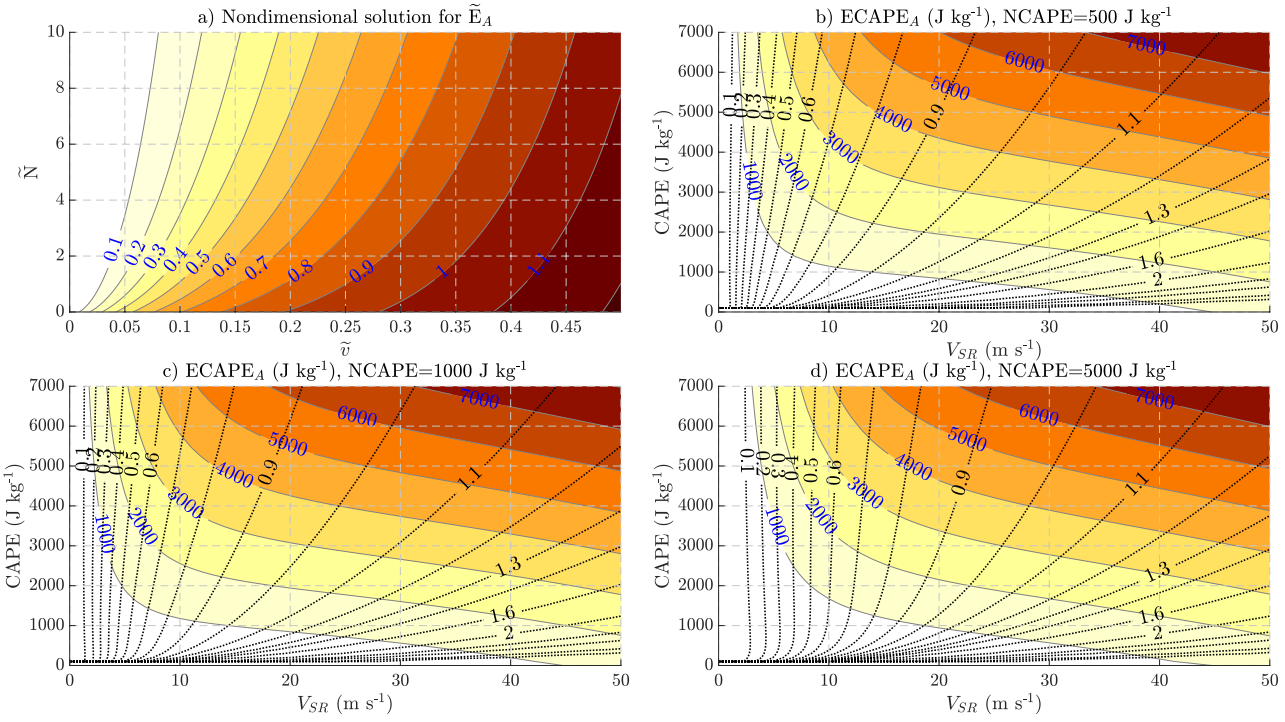

FIG. 6. Same as Fig. 6, but showing $\widetilde{E}_A$ (panel a), and ECAPE$_A$ (panels b-d).

The solution for $\widetilde{E}_A$ from eq. 52 (Fig. 6a) is similar to that of $\widetilde{E}$ from eq. 43 at small values of $\widetilde{v}$, but diverges notably from $\widetilde{E}$ at large $\widetilde{v}$, exceeding 1 (indicating that ECAPE$_A$ surpasses CAPE). Similar behavior is evident in the solutions for ECAPE$_A$ as a function of V_{SR} and CAPE (Fig. 6b-d). Notably, ECAPE$_A$ is similar to ECAPE at smaller values of V_{SR}, but larger than ECAPE$_A$ at large values of V_{SR}, which is evident as a persistent downward slant of ECAPE$_A$ as one moves from left-to-right on the figure. Again, we see that drastically different combinations of V_{SR} and CAPE can yield the same value of ECAPE$_A$. For instance, an environment with NCAPE of 500 J kg^{-1}, 1000 J kg^{-1} of CAPE, and a V_{SR} of 45 m s^{-1} will have an ECAPE$_A$ of 2000 J kg^{-1}. A starkly contrasting environment with NCAPE of 5000 J kg^{-1}, 7000 J kg^{-1} of CAPE, and a V_{SR} of 7 m s^{-1} will also have an ECAPE$_A$ of 2000 J kg^{-1}.

Accepted for publication in *Journal of the Atmospheric Sciences*. DOI 10.1175/JAS-D-23-0003.1.

To illustrate the circumstances under which pressure accelerations (as they have been formulated here) have the greatest enhancement effect on updrafts, we examine the quantity $F = \sqrt{\frac{\text{ECAPE}_A}{\text{ECAPE}}} - 1$, which is equal to the ratio of the fractional enhancement in w_{max} due to pressure accelerations in Fig. 7. Fractional enhancement is quite small (< 0.1) for most combinations of V_{SR} and CAPE. It only becomes larger than 0.1 for smaller values of CAPE and/or larger values of V_{SR}. Physically, when CAPE is large and/or V_{SR} is small, the kinetic energy generation from buoyancy dominates the updraft kinetic energy budget. Whereas, when CAPE is small and/or V_{SR} is large, the kinetic energy input from the environmental wind becomes comparable to the kinetic energy generation from buoyancy. Given this distribution of F, a potential explanation for why many past studies have found that w_{max} is primarily determined by buoyancy is that the CAPE and V_{SR} in these simulations fell within the region of the parameter space where F is small. In other words, the kinetic energy input into the updraft via the background environmental flow is insignificant compared to the kinetic energy generation via the release of CAPE in most storm environments.

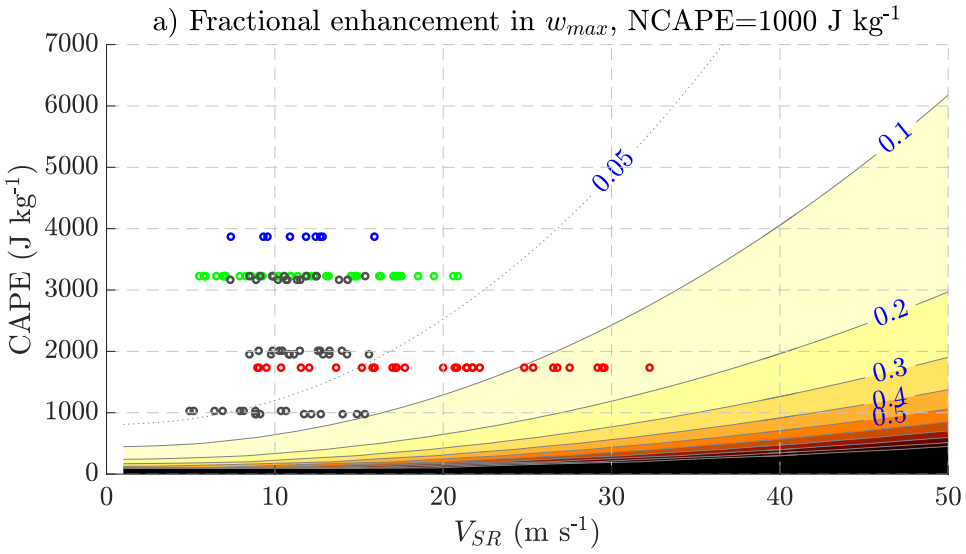

FIG. 7. F (shading, nondimensional) as a function of V_{SR} (x axis, m s^{-1}) and CAPE (y axis, J kg^{-1}). Colored dots indicate the V_{SR} and CAPE from the simulated storms analyzed in section 4.

Accepted for publication in *Journal of the Atmospheric Sciences*. DOI 10.1175/JAS-D-23-0003.1.

3. Evaluation of the formulas

a. Implementation of formula

The ECAPE formula derived in the previous section takes as input a single atmospheric profile of temperature, pressure, water vapor, and wind, and several constants with recommended values listed blow. We recommend using the following steps to compute this quantity in a software routine:

1. Set the following constant values: $c_p = 1005$ J kg^{-1} K^{-1}, $L_{v,r} = 2{,}501{,}000$ J kg^{-1}, $g = 9.81$ m s^{-1}, $\sigma = 1.1$, $\alpha = 0.8$, $k^2 = 0.18$, $P_r = \frac{1}{3}$, and $L_{mix} = 120$ m.

2. Compute CAPE, the LFC, and the H for an undiluted parcel from an atmospheric profile using an existing software routine (e.g., SHARPy, Metpy).

3. Compute the following parameter:

$$\psi = \frac{k^2 \alpha^2 \pi^2 L_{mix}}{P_r \sigma^2 H}, \tag{53}$$

   where H is the equilibrium level.

4. Compute V_{SR} from an atmospheric profile. We recommend averaging V_{SR} in the 0-1 km layer, using the method for estimating storm motion described by Bunkers et al. (2000).

5. Evaluate the following formula, using a numerical integration scheme.

$$\widehat{h_0}(z) = \frac{1}{z} \int_{z^*=0}^{z^*=z} \left(c_{pd} T_0 + L_{v,r} q_0 + g z^* \right) dz^*, \tag{54}$$

   This procedure only needs to be done once in a given profile, and yields $< h_0 >$ as a function of height.

6. Compute NCAPE, using the following formula:

$$\text{NCAPE} = - \int_{z=LFC}^{z=EL} \frac{g}{c_{pd} T_0} \left(\widehat{h_0} - h_0^* \right) dz, \tag{55}$$

Accepted for publication in *Journal of the Atmospheric Sciences*. DOI 10.1175/JAS-D-23-0003.1.

NCAPE is positive in most contexts though it may become negative in environments with large free tropospheric relative humidity. In the case of negative NCAPE, set this quantity to zero.

7. Nondimensionalize quantities: $\widetilde{v} = \frac{V_{SR}}{\sqrt{2CAPE}}$, $\widetilde{N} = \frac{NCAPE}{CAPE}$.

8. Compute nondimensional entraining CAPE ($\widetilde{E}_A$), using the following formula:

$$\widetilde{E}_A = \widetilde{v}^2 + \frac{-1-\psi-\frac{\psi}{\widetilde{v}^2}\widetilde{N}+\sqrt{\left(1+\psi+\frac{\psi}{\widetilde{v}^2}\widetilde{N}\right)^2+4\frac{\psi}{\widetilde{v}^2}\left(1-\psi\widetilde{N}\right)}}{2\frac{\psi}{\widetilde{v}^2}}, \tag{56}$$

This quantity represents the fraction of undiluted CAPE realized by an updraft. In the case of a negative solution to this equation, set the $\widetilde{E}_A$ to 0.

9. Compute dimensional entraining CAPE as $ECAPE_A = \widetilde{E}_A CAPE$.

Matlab and Python examples of this routine are provided at the link in the data availability statement.

b. Comparison of predicted w_{max} with the output from past simulations

We evaluate the accuracy of the formulas derived in the previous section by using them to predict the vertical velocities from simulations. The simulations, which featured a mix of supercells and multicellular clusters, originate from four past studies: Coffer et al. (2022) (C23, 9 simulations), Peters et al. (2023) (P23, 32 simulations), Peters et al. (2020c) (P20, 48 simulations), and Peters et al. (2019) (54 simulations). All simulations used Cloud Model 1 (CM1 Bryan and Fritsch 2002) and were initialized with soundings that featured a variety of different wind and thermodynamic profiles. Convection initiation in these simulations was generally driven by warm bubbles and updraft nudging methods, and no surface fluxes or radiation was used. Additional details of the model configurations are available in Table 1, along with the studies referenced in this paragraph.

We computed all subsequent quantities with the initial model thermodynamic and wind profiles and storm motions in past simulations. Predictions of w_{max} were derived using $w_{max} = \sqrt{2CAPE}$ and $w_{max} = \sqrt{2ECPE}$. We compared the predicted values of w_{max} to the temporal median of the instantaneous domain-wide w_{max} from the cm1out stats files during the 1-3 hour time range in the simulations, excluding tornadic periods in the P23 and C23 simulations (see those studies for

Accepted for publication in *Journal of the Atmospheric Sciences*. DOI 10.1175/JAS-D-23-0003.1.

TABLE 1. Summary of model configurations from past studies. Δx and Δz denote horizontal and vertical grid spacing, with a range of vertical grid spacing indicating a stretched grid. The "updraft tracking info" column references the page (P) abd section (S) in the referenced study that describes how updrafts were tracked.

Origin study	Δx	Δz	Domain horiz and vert. extent	Initiation method	Updraft tracking info.	LBC
Coffer et al. (2022)	80 m	20-280 m	100 x18 km	heat flux	P: 5, S: 2c1	semi-slip
Peters et al. (2023)	100 m	25-250 m	100 x 20 km	updraft nudging	P: 235, S: 2c	semi-slip
Peters et al. (2020c)	250 m	100 m	100 x 20 km	warm bubble	P: 3041 S: 3d	free-slip
Peters et al. (2019)	250 m	100 m	100 x 18 km	warm bubble	P: 3173 S: 2b	free-slip

definitions of "tornadic periods"). The parameter V_{SR} was computed by subtracting the tracked motion vector of simulated updrafts from the initial model profile, and averaging the resulting storm-relative wind profile in the 0-1 km layer. Other layer averages, including 0-500 m, 0-2 km, 0-3 km, and the density weighted average from the surface to the EL gave nearly identical results.

We will first see how well $\sqrt{2\text{CAPE}}$, which is the traditional "thermodynamic speed limit", predicts w_{max} (Fig. 8a). In this case, we calculate CAPE using the benchmark adiabatic parcel described in the beginning of section 2. This parameter loosely captures the differences in w_{max} among groups of simulations, but does not capture any of the variability in w_{max} among simulations that shared the same CAPE. Most w_{max} were less than the traditional thermodynamic speed limit (i.e., below the 1-to-1 line). However, the bulk of the P23 simulations and a few of the P19 simulations exceeded this threshold, by up to 15 m s^{-1}. The V_{SR} and CAPE of these simulations puts them in the portion of the parameter space where our theoretical representation of pressure effects predicts that their w_{max} should exceed $\sqrt{2\text{CAPE}}$ (see the gray and red dots in Fig. 7). The coefficient of determination (R^2) of $\sqrt{2\text{CAPE}}$ with simulated w_{max} was 0.38, with a root-mean-square-error (RMSE) of roughly 15 m s^{-1}.

To see if we can do a better job of predicting w_{max} with ECAPE that uses a fixed entrainment rate, we used a trial-and-error method to find the ε that yielded the smallest RMSE between predictions by eq. 25 and simulated w_{max} (this value was $\varepsilon = 2.25 \times 10^{-5}$ m^{-1}). This prediction reduces the RMSE to 12.2 m s^{-1}, but does not improve the R^2 much (Fig. 8b). Hence, with no knowledge of how the variations in environmental wind profiles affect entrainment, ECAPE with a fixed entrainment rate only slightly improves predictions of the mean w_{max} among groups of simulations, but does not capture any of the variance in w_{max} within a particular group.

Accepted for publication in *Journal of the Atmospheric Sciences*. DOI 10.1175/JAS-D-23-0003.1.

We *can* do a better job of predicting w_{max} by forming a mult-linear regression with $\sqrt{2\text{CAPE}}$, V_{SR}, and 3-7 km AGL mean relative humidity as predictors, and w_{max} as a predictand. This regression equation takes the form $w_{max,pred} = 0.7823\sqrt{2\text{CAPE}} + 1.503V_{SR} - 13.3437$. The predictions by this formula reduce RMSE to 7.95 m s^{-1} and increase the R^2 to 0.75 (Fig. 8c). This formula also produces an improved subjective correspondence between predicted and simulated w_{max}, but does not provide physical insight for the connections between these variables.

The ECAPE formula from P20, computed using all the procedures and parameter values described in that study, also better captures the variability in w_{max} among simulations with the same CAPE value than the $\sqrt{2\text{CAPE}}$ and ECAPE with a fixed entrainment rate, with a R^2 with w_{max} of 0.77. The RMSE of 12 m s^{-1}, however, is inferior to that of the linear regression and comparable to that of $\sqrt{2\text{CAPE}}$ and ECAPE with a fixed entrainment rate. This large error stems from a low bias in predictions from this formula, relative to the values in simulations, which is demonstrated by the dots mostly falling to the left of the one-to-one line in Fig. 8b). Recall that P20 used a $\varepsilon \sim R^{-1}$ scaling, and the buoyancy formula from that study consequently over-estimated the fractional reduction in undiluted buoyancy by entrainment. Both of these factors may have contributed to the formula's bias.

To evaluate the ECAPE and ECAPE$_\text{A}$ derived in the present study, we set L_{mix} = 120 m when evaluating the ECAPE formulas derived in the present study against the P23 and C23 simulations, and L_{mix} = 250 m when evaluating against the P20, N20, and P19 simulations to account for their coarser grid spacing. All other parameter values were the same as those used to generate Figs. 5-6. The new ECAPE formula improves correspondence (R^2 = 0.79), reduces the low bias in prediction, and substantially decreases RMSE (8.2 m s^{-1}) relative to the formula from P20 and the linear regression. The improvement over linear regression likely reflects an advantage of the nonlinear physical model underlying the ECAPE formula in capturing the nonlinear dependence of w_{max} on V_{SR}, CAPE, and entrainment. Dots in Fig. 8c fall close to the 1-1 line, suggesting that the $\varepsilon \sim R^{-2}$ scaling better reflects the trends in entrainment-driven dilution in the simulations than $\varepsilon \sim R^{-1}$.

The ECAPE$_\text{A}$ formula further improves correspondence between predicted and simulated w_{max} (R^2 = 0.82), decreases RMSE to 6.4 m s^{-1}, and brings points closer to the 1-to-1 line. The most notable difference between ECAPE$_\text{A}$ and ECAPE occurs with the P23 simulations, whose w_{max}

Accepted for publication in *Journal of the Atmospheric Sciences*. DOI 10.1175/JAS-D-23-0003.1.

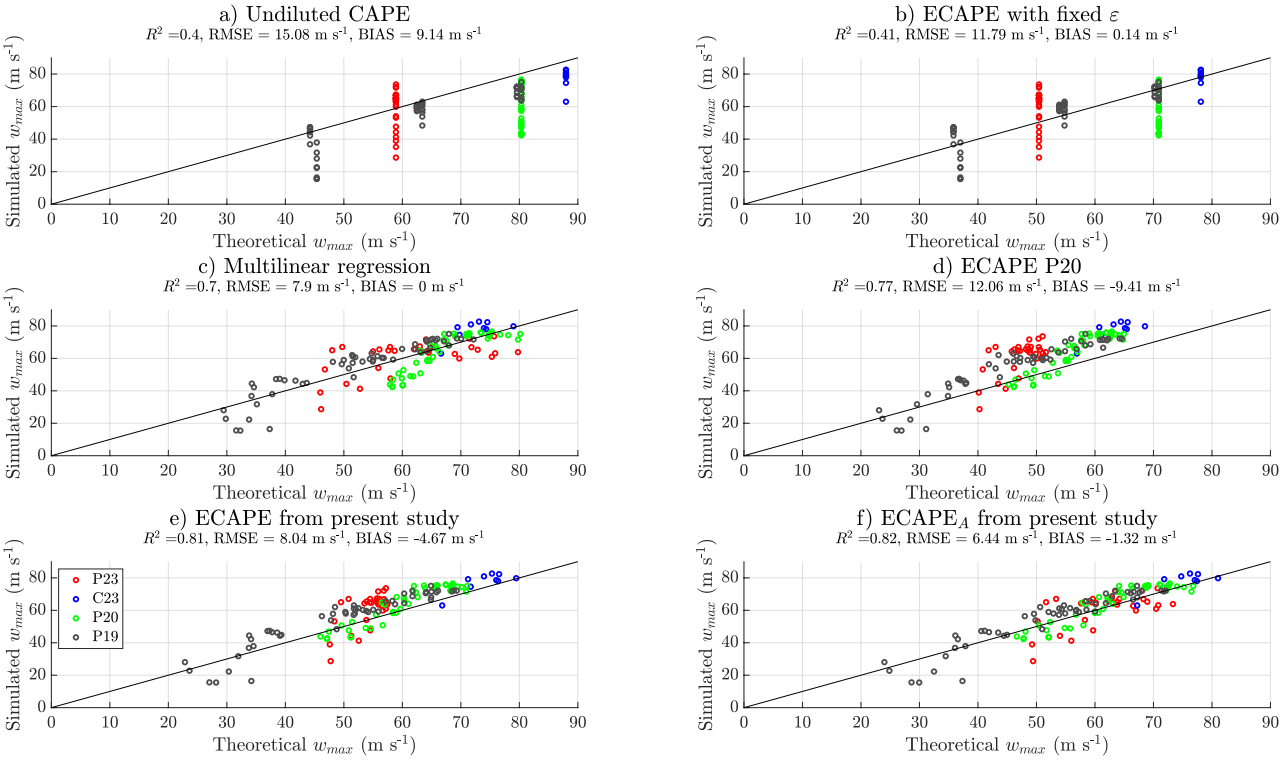

FIG. 8. All panels: predicted w_{max} (x axis, m s^{-1}) versus simulated w_{max} (y axis, m s^{-1}). Predictors are: the traditional "thermodynamic speed limit" $\sqrt{2\text{CAPE}}$ (panel a), ECAPE with the fixed ε that minimized the RMSE (panel b), a multi-linear regression with V_{SR} and $\sqrt{2\text{CAPE}}$ as predictors (panel c), ECAPE from P20 (panel d), ECAPE from the present study (panel e), and ECAPE$_\text{A}$ from the present study (panel f). Bias, RMSE and R^2 values are shown in the title of each plot. Colors correspond to the study where the simulations originated (see the legend in panel e).

substantially exceeded $\sqrt{2\text{CAPE}}$ (red dots above the 1-to-1 line in Fig. 8a) and was under-predicted by the ECAPE formulas from both P20 (red dots above the 1-to-1 line in Fig. 8b) and the present study (red dots above the 1-to-1 line in Fig. 8c). The ECAPE$_\text{A}$ brings the red dots much closer to the 1-to-1 line, correctly reflecting that w_{max} in many of these simulations exceeded $\sqrt{2\text{CAPE}}$.

The take home message is that the two formulas derived in the present study are superior predictors of w_{max} when compared to CAPE and ECAPE with a fixed entrainment rate. They also perform better than a simple linear regression that includes CAPE and V_{SR}, suggesting that the additional information contained in our formula about the environmental thermodynamic profile

Accepted for publication in *Journal of the Atmospheric Sciences*. DOI 10.1175/JAS-D-23-0003.1.

via the NCAPE parameter is critical to accurately representing the effects of entrainment on w_{max}. Finally, the new ECAPE formulas correct a low bias in the older P20 formula.

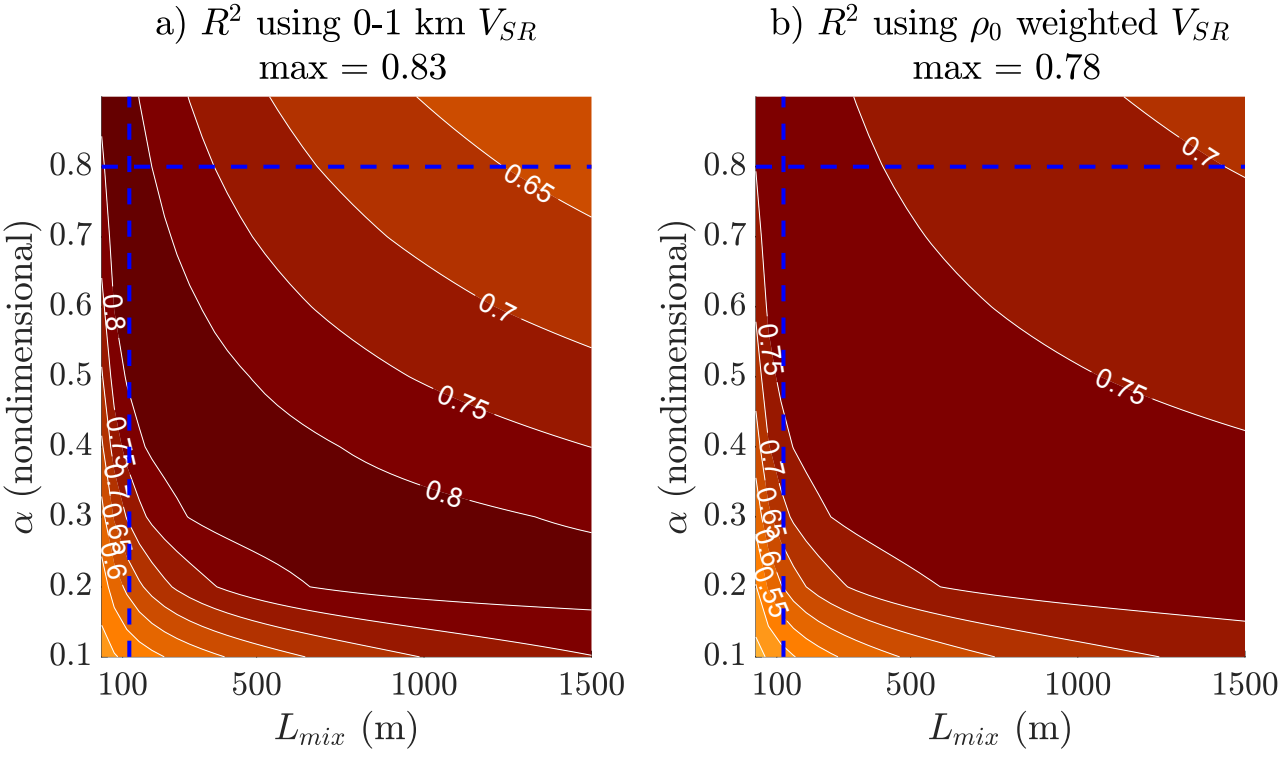

FIG. 9. Panel a: R^2 (shading) of w_{max} predicted from $ECAPE_A$ with w_{max} from simulations as a function of a range of L_{mix} (x axis, m) and α (y axis) values, where the formula is evaluated with the 0-1 km mean V_{SR}. The maximum R^2 for all α and L_{mix} is shown the panel title. Panel b: same as panel a, but with the ρ_0 weighted average of V_{SR} below the height of w_{max} in the simulated updrafts. Blue lines trace the L_{mix} = 120 m (vertical) and α = 0.8 (horizontal) values used in the study.

There are several "tunable parameters" contained within the ECAPE formula (e.g., L_{mix}, α, σ, the definition of V_{SR}), and their optimal values/configurations for producing a close fit to modeling data like that shown in Fig. 8 may vary due to a variety of factors, including model grid spacing, microphysics, differences between modeled and real-life updraft dynamics, and the mode of convection being analyzed (i.e., isolated updrafts, mesoscale convective systems). Hence, we emphasize that the important forecasting and research utility of ECAPE_A is the robustness of its ability to predict *relative* differences in updraft intensities among different environments. For example, Fig. 9 shows the R^2 of predicted w_{max} with that of the simulations we analyzed here for variety of L_{mix} and α values with the 0-1 km mean V_{SR} (panel a), and the mean ρ_0 weighted V_{SR}

Accepted for publication in *Journal of the Atmospheric Sciences*. DOI 10.1175/JAS-D-23-0003.1.

below the height of w_{max} in the simulations (panel b). Distributions of R^2 show broad regions of impressive R^2 (i.e., > 0.75), and all R^2 shown are substantially larger than the $R^2 = .4$ and $R^2 = 0.41$ for standard CAPE and ECAPE with a fixed ε respectively. This demonstrates that ECAPE$_A$ provides added value in terms of differentiating relative updraft intensities relative to traditional thermodynamic parameters *even when parameter values are not optimized* for a given dataset.

c. Properties of ECAPE in severe weather proximity soundings

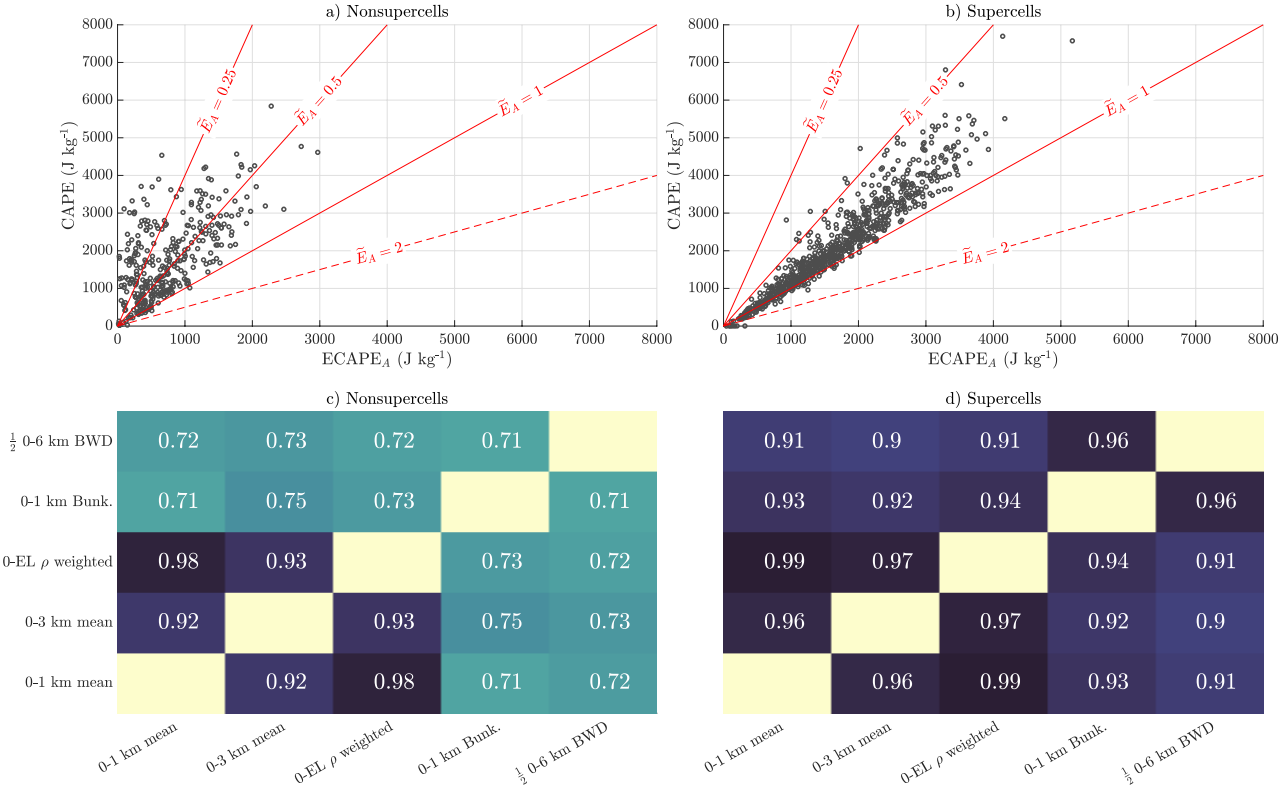

FIG. 10. Top panels: scatter plots of ECAPE$_A$ (x axis, J kg^{-1}) versus CAPE (y axis, J kg^{-1}), computed with the Thompson et al. (2003) soundings. Panel a: 351 nonsupercell events, and panel b: 834 supercell events. Contours of $\widetilde{E}_A$ are shown in red. Panels c-d: R^2 between solutions for ECAPE$_A$ computed using different definitions of V_{SR}. A given cell shows the correlation coefficient between ECAPE$_A$ computed with the V_{SR} definition on the x axis, with that on the corresponding y axis, with colors corresponding to the relative magnitudes.

Accepted for publication in *Journal of the Atmospheric Sciences*. DOI 10.1175/JAS-D-23-0003.1.

Our final analysis examines the distribution of ECAPE$_A$ within the Thompson et al. (2003) sounding dataset. Once again, we use the 0-1 km mean V_{SR} computed with the observed[9] storm motion in our formulas, though we evaluate other definitions of V_{SR} later in this sub-section. The distribution of ECAPE$_A$ for all nonsupercell severe weather events is plotted against undiluted CAPE in Fig. 10a. Contours of $\widetilde{E}_A$ (the fraction of CAPE "realized") are also shown for reference. There is substantial variability $\widetilde{E}_A$, with ECAPE$_A \approx$ CAPE ($\widetilde{E}_A \approx 1$) in some events, and ECAPE$_A <<$ CAPE ($\widetilde{E}_A << 1$) in others. Furthermore, case-to-case variations in ECAPE$_A$ and CAPE only loosely corresponded with one another, with $R^2 = 0.46$ based on a linear fit of these two quantities. In most events, particularly those with significant CAPE (> 1000 J kg^{-1}), ECAPE$_A$ was less than CAPE because of the typically smaller V_{SR} in nonsupercell environments. This suggests that most nonsupercell storms only realize a fraction of their available CAPE.

In contrast with nonsupercell events, there is a much closer correspondence between ECAPE$_A$ and CAPE in supercell events, with $R^2 = 0.90$ between these two variables (Fig. 10b). Furthermore, $\widetilde{E}_A > 0.5$ for nearly every supercell sounding, and this quantity was close to 1 in many cases, and exceeded 1 in a handful of instances. This corroborates the idea, proposed by Peters et al. (2019), that supercells realize a larger percentage of their environmental CAPE than nonsupercells. The primary reason for this difference is the larger vertical wind shear, and consequently storm-relative flow, in supercell environments relative to nonsupercell environments. Hence, CAPE may be a better predictor of storm-to-storm variations in updraft intensity in supercells than it is in nonosupercells. However, there is still substantial variability in the correspondence between ECAPE and CAPE, particular for larger CAPE values, which suggests that ECAPE provides added value over CAPE in supercell environments.

To evaluate the sensitivity of ECAPE to how V_{SR} is calculated, we re-computed ECAPE$_A$ with the 0-3 km mean V_{SR} with the observed storm motion, the density weighted average of V_{SR} below the LFC with the observed storm motion, the 0-1 km mean V_{SR} computed using the storm motion estimate of Bunkers et al. (2000) which estimates the advective storm motion component using the 0-6 km mean wind vector and propagation using an ad-hoc additive vector that is oriented perpendicular to the 0-6 km wind shear, and the advective storm motion only using half the 0-6 km bulk wind difference. Results with the V_{SR} measures that use the observed storm motion (i.e.,

[9]Observed storm motions in the Thompson et al. (2003) were determined via manual tracking of storm cells in radar imagery.

Accepted for publication in *Journal of the Atmospheric Sciences*. DOI 10.1175/JAS-D-23-0003.1.

the lower-left of Fig. 10c-d) yield R^2 in both nonsupercells (Fig. 10c) and supercells (Fig. 10d), with values ranging from 0.96 to 0.99.

In the case of supercells, the ECAPE_A computed with the observed storm motion corresponded well with the ECAPE_A computed using the Bunkers storm motion estimate and half the bulk wind difference (Fig. 10d). However, this correspondence was degraded slightly in nonsupercell events, with the R^2 ranging form 0.71 to 0.75 between ECAPE_A computed with the observed storm-motion, with that computed using the bunkers estimate and bulk wind difference. This result indicates that the motion of nonsupercell storms is more often influenced by extraneous factors like outflow and airmass boundaries, than in supercells. Hence, sounding-based estimates for storm motion do not correspond with actual storm motions as well in nonsupercell events as they do in supercell events. In many contexts where this formula would be used, such as in forecasting, the storm motion is unknown and must be estimated. This analysis suggests that estimating storm motion with the method of Bunkers et al. (2000) or half the 0-6 km BWD are both viable choices.

4. Summary, conclusions, and discussion

In summary, we have derived a formula for ECAPE that depends entirely on state variables available within an atmospheric sounding. This formula relies on three concepts: a scaling between fractional entrainment and updraft radius of $\varepsilon \sim R^{-2}$, the adiabatic conservation of moist static energy, and a direct correspondence between the cloud relative flow and the updraft radius. Finally, we have accounted for the potential enhancement of updraft kinetic energy via pressure accelerations.

Our results show that ECAPE provides a more accurate prediction of updraft intensity than standard CAPE when forecasting severe weather hazards that depend on middle-to-upper tropospheric vertical velocities. Examples of these situations include forecasting heavy precipitation, large hail, and intense cold pools and downdrafts. Hence, it would benefit the forecasting community to display this quantity alongside standard CAPE on websites that provide numerical weather prediction model output graphics, such as the storm-prediction center Mesoanalysis site. In addition, $\widetilde{E}_A$, which is the fraction of CAPE realized, is a powerful discriminator of supercellular from nonsupercellular storm mode, with a True Skill Statistic (TSS; e.g., section 2 in Peters et al. 2020c) of 0.76 in this prediction. This is on par with the TSS for 0-1 km V_{SR}, which is 0.79 (these values

Accepted for publication in *Journal of the Atmospheric Sciences*. DOI 10.1175/JAS-D-23-0003.1.

are not statistically different). The physical reason behind this discriminatory skill relates to the conclusions of Peters et al. (2019), who showed that supercells realize larger fractions of their CAPE than nonsupercells (and hence have larger $\widetilde{E}_A$).

A variety of research applications would also benefit from the consideration of ECAPE, in addition to standard CAPE. For instance, studies in past literature often contrast storm dynamics in high-shear low-CAPE severe weather events with events (e.g., Schneider and Dean 2008) occurring in environments with higher CAPE (and sometimes weaker shear). The premise behind this distinction is, because of the small updraft buoyancy in low-CAPE events, the updrafts accelerations in these storms are dominated by dynamic pressure accelerations rather than buoyancy (Wade and Parker 2021). However, it is possible that because of the extreme shear and storm-relative flow in many low-CAPE severe weather outbreaks, updrafts in these scenarios realize a higher percentage of their CAPE than their counterparts in high CAPE environments with weaker shear, because of the wider updrafts and reduced entrainment-driven dilution in the low-CAPE environments. Hence, ECAPE may more accurately distinguish between storms with large and small buoyancy than standard CAPE, and a reconsideration of the analyses in these past studies with distinctions drawn between high ECAPE and low ECAPE events may yield additional insights into storm dynamics.

ECAPE may also yield novel insight into the influence of climate change on thunderstorms. For instance, a subset of studies that investigate the influence of climate change on severe storm behavior use proxy analyses in global climate model (GCM) simulations, assessing the impacts of global warming on parameters like CAPE and CIN. Future changes to free tropospheric relative humidity, temperature, and vertical wind shear are also likely to influence thunderstorms via the connection between these environmental attributes and entrainment. Investigating changes to the climatology of ECAPE in future climates is a concise way of encapsulating these yet-to-be explored climate change influences on storm entrainment, and consequently storm intensity. Efforts to quantify the effects of climate change among the authors of the present study are currently underway.

Some of the intermediary formulas that express buoyancy and ECAPE as an analytic function of fractional entrainment may be useful in cumulus parameterization schemes. For instance, multi-plume schemes like the scheme of Arakawa and Schubert (1974), the Relaxed Arakawa-Schubert scheme (Moorthi and Suarez 1992), the EDMF^N scheme (Neggers 2015), and the MAP scheme

Accepted for publication in *Journal of the Atmospheric Sciences*. DOI 10.1175/JAS-D-23-0003.1.

(Peters et al. 2021) require the computation of diluted buoyancy and ECAPE for each plume. In the traditional approach for computing ECAPE, these schemes would execute two numerical integrations for each plume. This procedure, however, is dramatically simplified by using eq. 25 in the present study, where only 3 vertical integrations per grid cell are needed to obtain CAPE and NCAPE, and then the ECAPE associated with each plume is computed analytically. The MAP scheme from (Peters et al. 2021) was also formulated to use the formula from P20 as part of its closure for convective mass flux. The formula presented here is a more accurate alternative.

A potential caveat to using this parameter operationally is that ECAPE_A vanishes in the absence of V_{SR}, whereas we know that deep convection is possible in the absence of substantial V_{SR}. This discrepancy is likely a consequence of the primary controls on updraft width shifting away from vertical wind shear to other environmental factors when shear is weak, such as the planetary boundary layer (PBL) depth (e.g., Mulholland et al. 2021a) or the width scale of terrain features (e.g., Nelson et al. 2021; Kirshbaum 2022). Hence, the applicability of the present form of this formula in regions where weakly sheared deep convection (such as in the tropics) is unclear. A potential way to circumvent this issue is to revert to a standard ECAPE calculation (with a user-prescribed ε) in these weakly sheared environments, setting the updraft radius to scale with the PBL depth or to a constant value (e.g., 1500 m, as was done in Peters et al. 2021). A related caveat pertains to storm mode. The assumptions made in our theoretical derivation assume that updrafts are isolated and hence our results are most applicable to isolated updrafts. However, there is evidence that the connection between V_{SR} and updraft width also applies to mesoscale convective systems (MCSs, Mulholland et al. 2021b), and hence this formula may be applicable in MCS environments as well. Future work will address this possibility. Finally, the ECAPE_A could easily be modified to "elevated" storm environments by simply using the MUCAPE in the calculation and calculating V_{SR} within the effective inflow layer. Future work will consider this possibility.

Accepted for publication in *Journal of the Atmospheric Sciences*. DOI 10.1175/JAS-D-23-0003.1.

Acknowledgments. We are grateful for extremely helpful feedback from Zachary J. Lebo, Martin S. Singh, and an anonymous peer reviewer on an earlier version of this manuscript. J. Peters's efforts were supported by National Science Foundation (NSF) grants AGS-1928666, AGS-1841674, and the Department of Energy Atmospheric System Research (DOE ASR) grant DE-SC0000246356. D. Chavas was supported by National Science Foundation (NSF) grants 1648681 and 2209052. H. Morrison was supported by DOE ASR grant DE-SC0020104. The National Center for Atmospheric Research is sponsored by NSF. Finally, we thank Rich Thompson (NOAA SPC) for providing the Thompson et al. (2003) datset.

Data availability statement. Python and matlab code to compute ECAPE using an atmospheric sounding as input is available at https://doi.org/10.6084/m9.figshare.21859818.

References

Ahmed, F., and J. D. Neelin, 2018: Reverse engineering the tropical precipitation-buoyancy relationship. *J. Atmos. Sci.*, **75**, 1587–1608.

Arakawa, A., and W. H. Schubert, 1974: Interaction of a Cumulus Cloud Ensemble with the Large-Scale Environment, Part I. *J. Atmos. Sci.*, **31**, 674–701.

Betts, A. K., 1975: Parametric interpretation of trade-wind cumulus budget studies. *J. Atmos. Sci.*, **32**, 1934–1975.

Bolton, D., 1980: The computation of equivalent potential temperature. *Monthly Weather Review*, **108 (7)**, 1046 – 1053, https://doi.org/10.1175/1520-0493(1980)108⟨1046:TCOEPT⟩2.0.CO;2, URL https://journals.ametsoc.org/view/journals/mwre/108/7/1520-0493_1980_108_1046_tcoept_2_0_co_2.xml.

Brown, R. G., and C. Zhang, 1997: Variability of midtropospheric moisture and its effect on cloud-top height distribution during toga coare*. *Journal of the Atmospheric Sciences*, **54 (23)**, 2760 – 2774, https://doi.org/10.1175/1520-0469(1997)054⟨2760:VOMMAI⟩2.0.CO;2, URL https://journals.ametsoc.org/view/journals/atsc/54/23/1520-0469_1997_054_2760_vommai_2.0.co_2.xml.

Bryan, G. H., and J. M. Fritsch, 2002: A benchmark simulation for moist nonhydrostatic numerical models. *Mon. Wea. Rev.*, **130**, 2917–2928.

Accepted for publication in *Journal of the Atmospheric Sciences*. DOI 10.1175/JAS-D-23-0003.1.

Bryan, G. H., and R. Rotunno, 2014: The optimal state for gravity currents in shear. *J. Atmos. Sci.*, **71**, 448–468.

Bunkers, M. J., B. A. Klimowski, R. L. Thompson, and M. L. Weisman, 2000: Predicting supercell motion using a new hodpograph technique. *Wea. Forecasting*, **15**, 61–79.

Böing, S. J., H. J. J. Jonker, W. A. Nawara, and A. P. Siebesma, 2014: On the deceiving aspects of mixing diagrams of deep cumulus convection. *Journal of the Atmospheric Sciences*, **71 (1)**, 56 – 68, https://doi.org/10.1175/JAS-D-13-0127.1, URL https://journals.ametsoc.org/view/journals/atsc/71/1/jas-d-13-0127.1.xml.

Coffer, B., M. Parker, J. Peters, and A. Wade, 2022: Supercell low-level mesocyclones: Origins of inflow and vorticity. arXiv, URL https://arxiv.org/abs/2210.03715, https://doi.org/10.48550/ARXIV.2210.03715.

Danielsen, E. F., R. Bleck, and D. A. Morris, 1972: Hail growth by stochastic collection in a cumulus model. *J. Atmos. Sci.*, **29**, 135–155.

De Rooy, W. C., and A. P. Siebesma, 2010: Analytic expressions for entrainment and detrainment in cumulus convection. *Quart. J. Roy. Meteor. Soc.*, **136**, 1216–1227.

De Rooy, W. C., and Coauthors, 2013: Entrainment and detrainment in cumulus convection: an overview. *Quart. J. Roy. Meteor. Soc.*, **139**, 1–19.

Deardorff, J. W., 1972: Numerical investigation of neutral and unstable planetary boundary layers. *Journal of Atmospheric Sciences*, **29 (1)**, 91 – 115, https://doi.org/https://doi.org/10.1175/1520-0469(1972)029⟨0091:NIONAU⟩2.0.CO;2, URL https://journals.ametsoc.org/view/journals/atsc/29/1/1520-0469_1972_029_0091_nionau_2_0_co_2.xml.

Emanuel, K. A., 1994: *Atmospheric Convection*. 588 pp, Oxford University Press, New York, NY.

Fiedler, B. H., 1994: The thermodynamic speed limit and its violation in axisymmetric numerical simulations of tornado-like vortices. *Atmosphere-ocean*, **32**, 335–359.

Grabowski, W. W., and H. Morrison, 2021: Supersaturation, buoyancy, and moist convective dynamics. https://doi.org/10.5194/acp-2021-472.

Accepted for publication in *Journal of the Atmospheric Sciences*. DOI 10.1175/JAS-D-23-0003.1.

Gregory, D., 2001: Estimation of entrainment rate in simple models of convective clouds. *Quart. J. Roy. Meteor. Soc.*, **127**, 53–72.

Hernandez-Deckers, D., and S. C. Sherwood, 2016: A numerical investigation of cumulus thermals. *J. Atmos. Sci.*, **73**, 4117–4136.

Jeevanjee, N., 2017: Vertical velocity in the gray zone. *J. Adv. Model. Earth Sys.*, **9**, URL https://doi.org/10.1002/2017MS001059.

Jeevanjee, N., and D. M. Romps, 2015: Effective Buoyancy, Inertial Pressure, and the Mechanical Generation of Boundary Layer Mass Flux by Cold Pools. *J. Atmos. Sci.*, **72**, 3199–3213.

Jo, E., and S. Lasher-Trapp, 2022: Entrainment in a simulated supercell thunderstorm. part ii: The influence of vertical wind shear and general effects upon precipitation. *Journal of the Atmospheric Sciences*, **79 (5)**, 1429 – 1443, https://doi.org/10.1175/JAS-D-21-0289.1, URL https://journals.ametsoc.org/view/journals/atsc/79/5/JAS-D-21-0289.1.xml.

Khairoutdinov, M., and D. A. Randall, 2003: Cloud resolving modeling of the ARM summer 1997 IOP: Model formulation, results, unscertainties, and sensitivities. *J. Atmos. Sci.*, **60**, 607–625.

Kirshbaum, D. J., 2022: Large-eddy simulations of convection initiation over heterogeneous, low terrain. *Journal of the Atmospheric Sciences*, **79 (4)**, 973 – 987, https://doi.org/10.1175/JAS-D-21-0197.1, URL https://journals.ametsoc.org/view/journals/atsc/79/4/JAS-D-21-0197.1.xml.

Kuo, H. L., 1962: On the controlling influences of eddy diffusion on thermal convection. *Journal of Atmospheric Sciences*, **19 (3)**, 236 – 243, https://doi.org/10.1175/1520-0469(1962)019⟨0236:OTCIOE⟩2.0.CO;2, URL https://journals.ametsoc.org/view/journals/atsc/19/3/1520-0469_1962_019_0236_otcioe_2_0_co_2.xml.

Kuo, Y.-H., and J. D. Neelin, 2022: Conditions for convective deep inflow. *Geophysical Research Letters*, **49 (20)**, e2022GL100 552, https://doi.org/https://doi.org/10.1029/2022GL100552, URL https://agupubs.onlinelibrary.wiley.com/doi/abs/10.1029/2022GL100552, e2022GL100552 2022GL100552, https://agupubs.onlinelibrary.wiley.com/doi/pdf/10.1029/2022GL100552.

Accepted for publication in *Journal of the Atmospheric Sciences*. DOI 10.1175/JAS-D-23-0003.1.

Lasher-Trapp, S., E. Jo, L. R. Allen, B. N. Engelsen, and R. J. Trapp, 2021: Entrainment in a simulated supercell thunderstorm. part i: The evolution of different entrainment mechanisms and their dilutive effects. *Journal of the Atmospheric Sciences*, **78 (9)**, 2725 – 2740, https://doi.org/10.1175/JAS-D-20-0223.1, URL https://journals.ametsoc.org/view/journals/atsc/78/9/JAS-D-20-0223.1.xml.

Lebo, Z., 2018: A numerical investigation of the potential effects of aerosol-induced warming and updraft width and slope on updraft intensity in deep convective clouds. *Journal of the Atmospheric Sciences*, **75 (2)**, 535 – 554, https://doi.org/10.1175/JAS-D-16-0368.1, URL https://journals.ametsoc.org/view/journals/atsc/75/2/jas-d-16-0368.1.xml.

Lebo, Z. J., and H. Morrison, 2015: Effects of horizontal and vertical grid spacing on mixing in simulated squall lines and implications for convective strength and structure. *Mon. Wea. Rev.*, **143**, 4355–4375.

Lin, Y., and M. R. Kumjian, 2022: Influences of cape on hail production in simulated supercell storms. *Journal of the Atmospheric Sciences*, **79 (1)**, 179 – 204, https://doi.org/10.1175/JAS-D-21-0054.1, URL https://journals.ametsoc.org/view/journals/atsc/79/1/JAS-D-21-0054.1.xml.

Marion, G. R., and R. J. Trapp, 2019: The dynamical coupling of convective updrafts, downdrafts, and cold pools in simulated supercell thunderstorms. *Journal of Geophysical Research: Atmospheres*, **124 (2)**, 664–683.

Moorthi, S., and M. J. Suarez, 1992: Relaxed arakawa-schubert. a parameterization of moist convection for general circulation models. *Monthly Weather Review*, **120 (6)**, 978 – 1002, https://doi.org/10.1175/1520-0493(1992)120⟨0978:RASAPO⟩2.0.CO;2, URL https://journals.ametsoc.org/view/journals/mwre/120/6/1520-0493_1992_120_0978_rasapo_2_0_co_2.xml.

Morrison, H., 2016a: Impacts of updraft size and dimensionality on the perturbation pressure and vertical velocity in cumulus convection, Part 1: Simple, generalized analytic solutions. *J. Atmos. Sci.*, **73**, 1441–1454.

Accepted for publication in *Journal of the Atmospheric Sciences*. DOI 10.1175/JAS-D-23-0003.1.

Morrison, H., 2016b: Impacts of updraft size and dimensionality on the perturbation pressure and vertical velocity in cumulus convection, Part 2: Comparison of theoretical and numerical solutions. *J. Atmos. Sci.*, **73**, 1455–1480.

Morrison, H., 2017: An analytic description of the structure and evolution of growing deep cumulus updrafts. *J. Atmos. Sci.*, **74**, 809–834.

Morrison, H., and J. M. Peters, 2018: Theoretical expressions for the ascent rate of moist convective thermals. *J. Atmos. Sci.*, **75**, 1699–1719.

Morrison, H., J. M. Peters, K. K. Chandrakar, and S. C. Sherwood, 2022: Influences of environmental relative humidity and horizontal scale of subcloud ascent on deep convective initiation. *Journal of the Atmospheric Sciences*, **79 (2)**, 337 – 359, https://doi.org/10.1175/JAS-D-21-0056.1, URL https://journals.ametsoc.org/view/journals/atsc/79/2/JAS-D-21-0056.1.xml.

Morrison, H., J. M. Peters, W. M. Hannah, A. C. Varble, and S. E. Giangrande, 2020: Thermal chains in ascending moist updrafts: Part 1: Theoretical description. *J. Atmos. Sci.*, **77 (11)**, 3637–3660.

Morrison, H., J. M. Peters, and S. C. Sherwood, 2021: Comparing growth rates of simulated moist and dry convective thermals. *Journal of the Atmospheric Sciences*, **78 (3)**, 797 – 816, https://doi.org/10.1175/JAS-D-20-0166.1, URL https://journals.ametsoc.org/view/journals/atsc/78/3/JAS-D-20-0166.1.xml.

Mulholland, J. P., J. M. Peters, and H. Morrison, 2021a: How does lcl height influence deep convective updraft width? *Geophysical Research Letters*, **48 (13)**, e2021GL093 316, https://doi.org/https://doi.org/10.1029/2021GL093316, URL https://agupubs.onlinelibrary.wiley.com/doi/abs/10.1029/2021GL093316, e2021GL093316 2021GL093316, https://agupubs.onlinelibrary.wiley.com/doi/pdf/10.1029/2021GL093316.

Mulholland, J. P., J. M. Peters, and H. Morrison, 2021b: How does vertical wind shear influence entrainment in squall lines? *J. Atmos. Sci.*, **74**.

Mullendore, G. L., A. J. Homann, S. T. Jorgenson, T. J. Lang, and S. A. Tessendorf, 2013: Relationship between level of neutral buoyancy and dual-doppler observed mass detrainment levels in deep convection. *Atmos. Chem. Phys.*, **13**, 181–190.

Accepted for publication in *Journal of the Atmospheric Sciences*. DOI 10.1175/JAS-D-23-0003.1.

Neggers, R. A., 2015: Exploring bin-macrophysics models for moist convective transport and clouds. *J. Adv. Model. Earth Sys.*, **7**, 2079–2104.

Nelson, T. C., J. N. Marquis, J. M. Peters, and K. Friedrich, 2021: Cloud-scale simulations of convection initiation using observed near-cloud environments from RELAMPAGO-CACTI. *J. Atmos. Sci.*, **Accepted**.

Nowotarski, C. J., J. M. Peters, and J. P. Mulholland, 2020: Evaluating the effective inflow layer of simulated supercell updrafts. *J. Atmos. Sci.*, **148**, 3507–3532.

Parker, M. D., 2014: Composite VORTEX2 supercell environments from near-storm soundings. *Mon. Wea. Rev.*, **142**, 508–529.

Peters, J. M., 2016: The impact of effective buoyancy and dynamic pressure forcing on vertical velocities within 2 dimensional updrafts. *J. Atmos. Sci.*, **73**, 4531–4551.

Peters, J. M., and D. R. Chavas, 2021: Evaluating the conservation of energy variables in simulations of deep moist convection. *Journal of the Atmospheric Sciences*, **78 (10)**, 3229 – 3246, https://doi.org/10.1175/JAS-D-20-0351.1, URL https://journals.ametsoc.org/view/journals/atsc/78/10/JAS-D-20-0351.1.xml.

Peters, J. M., B. E. Coffer, M. D. Parker, C. J. Nowotarski, J. P. Mulholland, C. J. Nixon, and J. T. Allen, 2023: Disentangling the influences of storm-relative flow and horizontal streamwise vorticity on low-level mesocyclones in supercells. *Journal of the Atmospheric Sciences*, **80 (1)**, 129 – 149, https://doi.org/10.1175/JAS-D-22-0114.1, URL https://journals.ametsoc.org/view/journals/atsc/80/1/JAS-D-22-0114.1.xml.

Peters, J. M., H. Morrison, T. C. Nelson, J. N. Marquis, J. P. Mulholland, and C. J. Nowotarski, 2022a: The influence of shear on deep convection initiation. part i: Theory. *Journal of the Atmospheric Sciences*, **79 (6)**, 1669 – 1690, https://doi.org/10.1175/JAS-D-21-0145.1, URL https://journals.ametsoc.org/view/journals/atsc/79/6/JAS-D-21-0145.1.xml.

Peters, J. M., H. Morrison, T. C. Nelson, J. N. Marquis, J. P. Mulholland, and C. J. Nowotarski, 2022b: The influence of shear on deep convection initiation. part ii: Simulations. *Journal of the Atmospheric Sciences*, **79 (6)**, 1691 – 1711, https://doi.org/10.1175/JAS-D-21-0144.1, URL https://journals.ametsoc.org/view/journals/atsc/79/6/JAS-D-21-0144.1.xml.

Accepted for publication in *Journal of the Atmospheric Sciences*. DOI 10.1175/JAS-D-23-0003.1.

Peters, J. M., H. Morrison, C. J. Nowotarski, J. P. Mulholland, and R. L. Thompson, 2020a: A formula for the maximum vertical velocity in supercell updrafts. *J. Atmos. Sci.*, **77 (11)**, 3747–3757.

Peters, J. M., H. Morrison, G. J. Zhang, and S. W. Powell, 2021: Improving the physical basis for updraft dynamics in deep convection parameterizations. *Journal of Advances in Modeling Earth Systems*, **13 (2)**, e2020MS002 282, https://doi.org/https://doi.org/10.1029/2020MS002282, URL https://agupubs.onlinelibrary.wiley.com/doi/abs/10.1029/2020MS002282, e2020MS002282 2020MS002282, https://agupubs.onlinelibrary.wiley.com/doi/pdf/10.1029/2020MS002282.

Peters, J. M., J. P. Mulholland, and D. R. Chavas, 2022c: Generalized lapse rate formulas for use in entraining cape calculations. *Journal of the Atmospheric Sciences*, **79 (3)**, 815 – 836, https://doi.org/10.1175/JAS-D-21-0118.1, URL https://journals.ametsoc.org/view/journals/atsc/79/3/JAS-D-21-0118.1.xml.

Peters, J. M., C. Nowotarski, and H. Morrison, 2019: The role of vertical wind shear in modulating maximum supercell updraft velocities. *J. Atmos. Sci.*, **76**, 3169–3189.

Peters, J. M., C. Nowotarski, and G. Mullendore, 2020b: Are supercells resistant to entrainment because of their rotation? *J. Atmos. Sci.*, **77**, 1475–1495.

Peters, J. M., C. J. Nowotarski, and J. P. Mulholland, 2020c: The influences of effective inflow layer streamwise vorticity and storm-relative flow on supercell updraft properties. *J. Atmos. Sci.*, **77**, 3033–3057.

Politovich, M. K., and W. A. Cooper, 1988: Variability of the supersaturation in cumulus clouds. *Journal of Atmospheric Sciences*, **45 (11)**, 1651 – 1664, https://doi.org/10.1175/1520-0469(1988)045⟨1651:VOTSIC⟩2.0.CO;2, URL https://journals.ametsoc.org/view/journals/atsc/45/11/1520-0469_1988_045_1651_votsic_2_0_co_2.xml.

Riehl, H., and J. S. Malkus, 1958: On the heat balance in the equatorial trough zone. *Geophysica*, **6**, 503–538.

Accepted for publication in *Journal of the Atmospheric Sciences*. DOI 10.1175/JAS-D-23-0003.1.

Romps, D. M., 2014: An analytical model for tropical relative humidity. *Journal of Climate*, **27 (19)**, 7432 – 7449, https://doi.org/https://doi.org/10.1175/JCLI-D-14-00255.1, URL https://journals.ametsoc.org/view/journals/clim/27/19/jcli-d-14-00255.1.xml.

Romps, D. M., 2015: Mse minus CAPE is the true conserved variable for an adiabatically lifted parcel. *J. Atmos. Sci.*, **72**, 3639–3646.

Romps, D. M., and A. B. Charn, 2015: Sticky Thermals: Evidence for a Dominant Balance between Buoyancy and Drag in Cloud Updrafts. *J. Atmos. Sci.*, **72**, 2890–2901.

Romps, D. M., and Z. Kuang, 2010a: Do undiluted convective plumes exist in the upper troposphere? *J. Atmos. Sci.*, **67**, 468–484.

Romps, D. M., and Z. Kuang, 2010b: Nature versus nurture in shallow convection. *J. Atmos. Sci.*, **67**, 1655–1666.

Romps, D. M., J. T. Seeley, D. Vollaro, and J. Molinari, 2014: Projected increase in lightning strikes in the united states due to global warming. *Science*, **346 (6211)**, 851–854, https://doi.org/10.1126/science.1259100, URL https://www.science.org/doi/abs/10.1126/science.1259100, https://www.science.org/doi/pdf/10.1126/science.1259100.

Schneider, R. S., and A. R. Dean, 2008: A comprehensive 5-year severe storm environment climatology for the continental united states. *Preprints, 24th Conf. on Severe Local Storms*, Amer. Meteor. Soc., 16A.4. [Available onlineathttps://ams.confex.com/ams/pdfpapers/141 748.pdf.].

Sherwood, S. C., D. Hernandez-Deckers, and M. Colin, 2013: Slippery thermals and the cumulus entrainment paradox. *J. Atmos. Sci.*, **70**, 2426–2442.

Singh, M. S., and P. A. O'Gorman, 2013: Influence of entrainment on the thermal stratification in simulations of radiative-convective equilibrium. *Geophysical Research Letters*, **40 (16)**, 4398–4403, https://doi.org/https://doi.org/10.1002/grl.50796, URL https://agupubs.onlinelibrary.wiley.com/doi/abs/10.1002/grl.50796, https://agupubs.onlinelibrary.wiley.com/doi/pdf/10.1002/grl.50796.

Squires, P., and J. S. Turner, 1962: An entraining jet model for cumulo-nimbus updrafts. *Tellus*, **14A**, 422–434.

Accepted for publication in *Journal of the Atmospheric Sciences*. DOI 10.1175/JAS-D-23-0003.1.

Stolz, D. C., S. A. Rutledge, and J. R. Pierce, 2015: Simultaneous influences of thermodynamics and aerosols on deep convection and lightning in the tropics. *J. Geophys. Res. Atm.*, **120**, 6207–6231.

Sueki, K., and H. Niino, 2016: Toward better assessment of tornado potential in typhoons: Significance of considering entrainment effects for cape. *Geophysical Research Letters*, **43 (24)**, 12,597–12,604, https://doi.org/https://doi.org/10.1002/2016GL070349, URL https://agupubs.onlinelibrary.wiley.com/doi/abs/10.1002/2016GL070349, https://agupubs.onlinelibrary.wiley.com/doi/pdf/10.1002/2016GL070349.

Takahashi, H., Z. J. Luo, and G. Stephens, 2021: Revisiting the entrainment relationship of convective plumes: A perspective from global observations. *Geophysical Research Letters*, **48 (6)**, e2020GL092 349, https://doi.org/https://doi.org/10.1029/2020GL092349, URL https://agupubs.onlinelibrary.wiley.com/doi/abs/10.1029/2020GL092349, e2020GL092349 2020GL092349, https://agupubs.onlinelibrary.wiley.com/doi/pdf/10.1029/2020GL092349.

Thompson, R. L., R. Edwards, J. A. Hart, K. L. Elmore, and P. Markowski, 2003: Close proximity soundings within supercell environments obtained from the Rapid Update Cycle. *Wea. Forecasting*, **18**, 1243–1261.

Thompson, R. L., C. M. Mead, and R. Edwards, 2007: Effective Storm-Relative Helicity and Bulk Shear in Supercell Thunderstorm Environments. *Wea. Forecasting*, **22**, 102–115.

Tochimoto, E., K. Sueki, and H. Niino, 2019: Entraining cape for better assessment of tornado outbreak potential in the warm sector of extratropical cyclones. *Monthly Weather Review*, **147 (3)**, 913 – 930, https://doi.org/10.1175/MWR-D-18-0137.1, URL https://journals.ametsoc.org/view/journals/mwre/147/3/mwr-d-18-0137.1.xml.

Wade, A. R., and M. D. Parker, 2021: Dynamics of simulated high-shear, low-cape supercells. *Journal of the Atmospheric Sciences*, **78 (5)**, 1389 – 1410, https://doi.org/10.1175/JAS-D-20-0117.1, URL https://journals.ametsoc.org/view/journals/atsc/78/5/JAS-D-20-0117.1.xml.

Weisman, M. L., and R. Rotunno, 2000: The Use of Vertical Wind Shear Versus Helicity in Interpreting Supercell Dynamics. *J. Atmos. Sci.*, **57**, 1452–1472, https://doi.org/http://dx.doi.org/10.1175/1520-0469(2000)057⟨1452:TUOVWS⟩2.0.CO;2.

Accepted for publication in *Journal of the Atmospheric Sciences*. DOI 10.1175/JAS-D-23-0003.1.

Zhang, G. J., 2009: Effects of entrainment on convective available potential energy and closure assumptions in convective parameterization. *J. Geophys. Res.*, **114**, D07 109.

Zipser, E. J., 2003: *Some Views On "Hot Towers" after 50 Years of Tropical Field Programs and Two Years of TRMM Data*, 49–58. American Meteorological Society, Boston, MA, https://doi.org/10.1007/978-1-878220-63-9_5, URL https://doi.org/10.1007/978-1-878220-63-9_5.

Accepted for publication in *Journal of the Atmospheric Sciences*. DOI 10.1175/JAS-D-23-0003.1.